

One-Pot Scalable Production of Conjugated Microporous Polymers with Exceptional Functionality

Duanlian Tang,^{# [a]} Zhuo Xiong,^{# [a]} John D. Worth,^[b] Ting Qiu^{[a]}, Charl F. J. Faul,^{*[b]}, and Jie Chen^{*[a]}*

^[a] D. Tang, Z. Xiong, Prof. T Qiu*, Prof. J. Chen*

Engineering Research Centre of Reactive Distillation, College of Chemical Engineering, Fuzhou University,
Fuzhou 350108, P. R. China

E-mail: tingqiu@fzu.edu.cn (Prof. T. Qiu); jiechen@fzu.edu.cn (Prof. J. Chen);

^[b] J. D. Worth, Prof. C. F. J. Faul

School of Chemistry, University of Bristol, Bristol, BS8 1TS, UK.

E-mail: charl.faul@bristol.ac.uk (Prof. C. F. J. Faul).

^[#] These authors contributed equally.

Table of Contents

Table of Contents	2
S1 Experimental Procedures.....	5
S1.1 Chemicals.....	5
S1.2 Synthesis of FZU-PTPA in the autoclave without degassing procedures under different temperatures.....	5
S1.3 Synthesis of FZU-PTPA in the autoclave without degassing procedures with different pressures.....	5
S1.4 Synthesis of FZU-PTPA in the autoclave without degassing procedures with different reaction times.....	5
S1.5 Synthesis of PTPA-Cl in the autoclave without degassing procedures	5
S1.6 Characterization.....	5
S1.7 Mercury ion adsorption experiment.....	6
S1.8 Methodology	6
S1.8.1 Kinetic study	6
S1.8.2 Isotherm study.....	6
S1.8.3 Thermodynamic study.....	7
S1.9 DFT calculation	7
S2 Results and discussion	8
S2.1 Successful coupling of 1,4-dichlorobenze and tri(4-aminophenyl) amine	8
S2.2 Doping in the PTPA-Cl.....	8
S2.3 Detection of the -NH ₂ from the XPS results.....	8
S2.4 Confirming the synthetic mechanism of the FZU approach from the Hansen-solubility-parameter point of view.....	8
S3 Supplementary Figures	9
Figure S1 Calculated ¹³ C NMR spectrum of the PTPA oligomer through the ChemDraw software package	9
Figure S2 FTIR spectra of FZU-PTPA synthesized under differential reaction temperature	10
Figure S3 FTIR spectra of FZU-PTPA, core (tri(4-bromophenyl) amine) and linker (phenylenediamine).....	11
Figure S4 TGA (a) and the corresponding DTGA (b) curves of the FTIR spectra of FZU-PTPA synthesized under differential reaction temperature	12
Figure S5 N ₂ adsorption isotherm (a), pore size distribution (PSD, b) and pore volume distribution (PV, c) of FZU-PTPA synthesized under differential temperature	13
Figure S6 (a)SS UV/Vis NIR spectra of FZU-PTPA under differential reaction temperature; (b)FTIR spectra of FZU-PTPA synthesized under differential reaction time.....	14
Figure S7 SS ¹³ C NMR spectra of FZU-PTPA synthesized under differential reaction time and pressure.....	15
Figure S8 N ₂ adsorption isotherm (a), pore size distribution (PSD, b) and pore volume distribution (PV, c) of FZU-PTPA synthesized under differential reaction time	16
Figure S9 TGA (a) and the corresponding DTG (b) curves of the FTIR spectra of FZU-PTPA synthesized under differential reaction time.....	17
Figure S10 SS UV/Vis NIR of FZU-PTPA synthesized under differential reaction time	18
Figure S11 SEM images of FZU-PTPA synthesized under differential reaction time	19
Figure S12 Synthesis of PTPA via Buchwald-Hartwig cross-coupling of 1,4-dibromobenzene and tris(4-aminophenyl)amine.	20
Figure S13 Synthesis of PTPA-Cl via Buchwald-Hartwig cross-coupling of 1,4-dichlorobenzene and tris(4-aminophenyl)amine.	21
Figure S14 FTIR spectra of FZU-PTPA (120 °C) and PTPA-Cl.....	22
Figure S15 FTIR spectra of FZU-PTPA synthesized under differential pressure of inserted N ₂	23
Figure S16 XRD spectra of FZU-PTPA (120 °C).....	24
Figure S17 XRD spectra of PTPA-Cl (120 °C).....	25
Figure S18 N ₂ adsorption isotherm (a), pore size distribution (PSD, b) and pore volume distribution (PV, c) of FZU-PTPA synthesized under differential pressure of inserted N ₂	26
Figure S19 TGA (a) and DTGA (b) curves of FZU-PTPA synthesized under differential pressure of inserted N ₂ 27	27

Figure S20 SS UV/Vis spectra of FZU-PTPA synthesized under differential pressure of inserted N ₂	28
Figure S21 SEM images of FZU-PTPA synthesized under differential pressure of inserted N ₂	29
Figure S22 SEM images of FZU-PTPA synthesized under differential reaction temperatures.....	30
Figure S23 illustration of the nucleate growth of PTPA synthesized in a poor polymerization process (for example, the process by using the conventional polymerization method) ⁴⁻⁶	31
Figure S24 illustration of the nucleate growth of PTPA synthesized in a favorable polymerization process (for example, the process by using the FZU polymerization method under a mild temperature) ⁴⁻⁶	32
Figure S25 illustration of the nucleate growth of PTPA synthesized in an over-fast polymerization process (for example, the process by using the FZU polymerization method under an over-high temperature) ⁴⁻⁶	33
Figure S26 the relationship between the reaction temperature and the specific surface area of PTPAs synthesis in different solvent	34
Figure S27 FTIR spectra of FZU-PTPA synthesized in toluene under differential temperature	35
Figure S28 N ₂ adsorption isotherm (a), pore size distribution (PSD, b) and pore volume distribution (PV, c) of FZU-PTPA synthesized in toluene under differential temperature	36
Figure S29 isosteric heat of adsorption (Q_{st}) of FZU-PTPA acquired in the Micromeritics ASAP 2020 HD88 based on the adsorption data conducted at 273 K and 298 K	37
Figure S30 fitting of kinetic data with the pseudo-first-order model of FZU-PTPA.....	38
Figure S31 fitting of kinetic data with the pseudo-second-order model of FZU-PTPA	39
Figure S32 fitting of isotherm data with the Langmuir model of FZU-PTPA	40
Figure S33 fitting of isotherm data with the Freundlich model of FZU-PTPA.....	41
Figure S34 fitting of thermodynamic data of FZU-PTPA.....	42
Figure S35 Selectivity coefficients of Hg(II) against other cations obtained from the batch adsorption experiments	43
Figure S36 The Hg(II) removal efficiency of our FZU-PTPA in a 5-cycles reuse	44
Figure S37 FTIR spectra of FZU-PTPA (120 °C) before and after mercury adsorption.....	45
Figure S38 full-scan XPS spectra of FZU-PTPA synthesized under different temperature.....	46
Figure S39 N1s XPS spectra of FZU-PTPA synthesized under different temperature	47
Figure S40 C1s XPS spectra of FZU-PTPA synthesized under different temperature.....	48
Figure S41 O1s XPS spectra of FZU-PTPA synthesized under different temperature	49
Figure S42 full-scan XPS spectra of FZU-PTPA synthesized under different pressure	50
Figure S43 N 1s XPS spectra of FZU-PTPA synthesized under different pressure	51
Figure S44 C 1s XPS spectra of FZU-PTPA synthesized under different pressure	52
Figure S45 O 1s XPS spectra of FZU-PTPA synthesized under different pressure	53
Figure S46 full-scan XPS spectra of FZU-PTPA synthesized under different reaction time.....	54
Figure S47 N 1s XPS spectra of FZU-PTPA synthesized under different reaction time	55
Figure S48 C 1s XPS spectra of FZU-PTPA synthesized under different reaction time	56
Figure S49 O 1s XPS spectra of FZU-PTPA synthesized under different reaction time	57
Figure S50 full-scan XPS spectra of FZU-PTPA (2 MPa, 120 °C, 5 h) and PTPA-Cl	58
Figure S51 C 1s XPS spectra of FZU-PTPA (2 MPa, 120 °C, 5 h) and PTPA-Cl	59
Figure S52 O 1s XPS spectra of FZU-PTPA (2 MPa, 120 °C, 5 h) and PTPA-Cl.....	60
Figure S53 full-scan XPS spectra of FZU-PTPA before and after mercury adsorption.....	61
Figure S54 N1s XPS spectra of FZU-PTPA (120 °C) before and after mercury adsorption	62
Figure S55 C1s XPS spectra of FZU-PTPA (120 °C) before and after mercury adsorption	63
Figure S56 O1s XPS spectra of FZU-PTPA (120 °C) before and after mercury adsorption	64
Figure S57 Hg 4d XPS spectra of FZU-PTPA (120 °C) after mercury adsorption.....	65
Figure S58 optimized structure of the oligomers of FZU-PTPA before (a) and after mercury adsorption (b) by Gaussian 16 W using a B3PW91/6-31g(d) basis set.	66
Figure S59 Information of molecular orbital (in a unit of a.u.) of an oligomer of FZU-PTPA calculated by Gaussian 16 W using a B3PW91/6-31g(d) basis set.	67
Figure S60 Information of molecular orbital (in a unit of a.u.) of an oligomer of FZU-PTPA after interaction with the mercury ions calculated by Gaussian 16 W using a B3PW91/6-31g(d) basis set.	68
S4 Supplementary tables	69

Table S1 peak positions and specific surface area of the SS UV/Vis spectra of FZU-PTPA.....	69
Table S2 CO ₂ adsorption capacity of advanced porous materials.....	70
Table S3 The isosteric heat of adsorption Q_{st} of various samples.....	71
Table S4 kinetic parameters of the FZU-PTPA (120 °C) towards the mercury ions fitted by the pseudo-first-order and pseudo-second-order model.....	72
Table S5 initial adsorption rate h of benchmark adsorbents.....	73
Table S6 isotherm parameters of the FZU-PTPA (120°C) towards the mercury ions fitted by the Langmuir and Freundlich model.....	74
Table S7 Properties of cations used in competitive adsorption experiments.....	75
Table S8 thermodynamic parameters of the FZU-PTPA (120 °C) towards the mercury ions.....	76
Table S9 adsorption capacity towards the mercury ions of other advanced porous materials.....	77
Table S10 XPS N1s spectra information of FZU-PTPA synthesized under differential temperature.....	78
Table S11 XPS C1s spectra information of FZU-PTPA synthesized under differential temperature.....	79
Table S12 XPS O1s spectra information of FZU-PTPA synthesized under differential temperature.....	80
Table S13 XPS N1s spectra information of FZU-PTPA synthesized under differential pressure.....	81
Table S14 XPS C1s spectra information of FZU-PTPA synthesized under differential pressure.....	82
Table S15 XPS O1s spectra information of FZU-PTPA synthesized under differential pressure.....	83
Table S16 XPS N1s spectra information of FZU-PTPA synthesized under differential reaction time.....	84
Table S17 XPS C1s spectra information of FZU-PTPA synthesized under differential reaction time.....	85
Table S18 XPS O1s spectra information of FZU-PTPA synthesized under differential reaction time.....	86
Table S19 XPS N1s spectra information of PTPA-Cl.....	87
Table S20 XPS C1s spectra information of PTPA-Cl.....	88
Table S21 XPS O1s spectra information of PTPA-Cl.....	89
Table S22 XPS N1s spectra information of FZU-PTPA before and after adsorption with the mercury ion.....	90
Table S23 XPS C1s spectra information of FZU-PTPA before and after adsorption with the mercury ion.....	91
Table S24 XPS O1s spectra information of FZU-PTPA before and after adsorption with the mercury ion.....	92
References:	93

S1 Experimental Procedures

S1.1 Chemicals

All chemical reagents were used without purification and dehydration. (Core) Tris(4-bromophenyl) amine; (linker) phenylenediamine or 1,4-dichlorobenzene; (catalyst) bis(dibenzylideneacetone) palladium (0) (Pd(dba)₂); (ligand) 2-dicyclohexylphosphino-2',4',6'-triisopropylbiphenyl (XPhos, 97%); (base) sodium tert-butoxide (NaOtBu, 97%) were of AR grades, which were purchased from Shanghai Aladdin Biochemical Technology Co., Ltd. Tetrahydrofuran (THF), trichloromethane, 1,4-dioxane, HgCl₂, Cu(NO₃)₂, Zn(NO₃)₂, La(NO₃)₂, Pb(NO₃)₂, Co(NO₃)₂, Ni(NO₃)₂, HCl and NaOH were of AR grades, which were purchased from Sinopharm (China) Chemical Reagent Co., Ltd.

S1.2 Synthesis of FZU-PTPA in the autoclave without degassing procedures under different temperatures

Compared to conventional synthetic procedures, our methodology using an autoclave showed a simple and facile nature. The starting materials, *i.e.*, *p*-phenylenediamine (1 mmol), tris(4-bromophenyl) amine (1 mmol), catalysts, *i.e.*, Pd(dba)₂ (0.05 mmol), XPhos (0.09 mmol) and NaOtBu (3.5 mmol), and the solvent THF (70 ml, AR, without any dehydration) were directly charged in a 100 mL autoclave for reaction without any tedious degassing operations, while 2 MPa of the N₂ was inserted. After the seal-up of the autoclave, the mixture was heated to 100–160 °C, respectively under the stirring allowing for the B–H coupling reaction for 5 h. The reactor was then cooled to room temperature, and the products were washed by 100 ml THF, CHCl₃, ethanol and hot water, respectively, and dried in a vacuum oven at 70 °C for 24 h. Notes these PTPAs were insoluble in the common organic solvents.

S1.3 Synthesis of FZU-PTPA in the autoclave without degassing procedures with different pressures

The starting materials, *i.e.*, *p*-phenylenediamine (1 mmol), tris(4-bromophenyl) amine (1 mmol), catalysts, *i.e.*, Pd(dba)₂ (0.05 mmol), XPhos (0.09 mmol) and NaOtBu (3.5 mmol), and the solvent THF (70 ml, AR, without any dehydration) were directly charged in a 100 mL autoclave without any tedious degassing operations. After the seal-up of the autoclave, the pressure was further increased from 0 MPa to 2 MPa, respectively using the N₂, and the mixture was then heated to 120 °C under the stirring allowing for the B–H coupling reaction for 16 h. The reactor was then cooled to room temperature, and the products were washed by 100 ml THF, CHCl₃, ethanol and hot water, respectively, and dried in a vacuum oven at 70 °C for 24 h.

S1.4 Synthesis of FZU-PTPA in the autoclave without degassing procedures with different reaction times

The starting materials, *i.e.*, *p*-phenylenediamine (1 mmol), tris(4-bromophenyl) amine (1 mmol), catalysts, *i.e.*, Pd(dba)₂ (0.05 mmol), XPhos (0.09 mmol) and NaOtBu (3.5 mmol), and the solvent THF (70 ml, AR, without any dehydration) were directly charged in a 100 mL autoclave without any tedious degassing operations, while 2 MPa of the N₂ was inserted. After the seal-up of the autoclave, the mixture was heated to 120 °C under the stirring allowing for the B–H coupling reaction for 1 h, 5 h and 16 h, respectively. The reactor was then cooled to room temperature, and the products were washed by 100 ml THF, CHCl₃, ethanol and hot water, respectively, and dried in a vacuum oven at 70 °C for 24 h.

S1.5 Synthesis of PTPA-Cl in the autoclave without degassing procedures

The starting materials, *i.e.*, 1,4-dichlorobenzene (1 mmol), tris(4-bromophenyl) amine (1 mmol), catalysts, *i.e.*, Pd(dba)₂ (0.05 mmol), XPhos (0.09 mmol) and NaOtBu (3.5 mmol), and the solvent THF (70 ml, AR, without any dehydration) were directly charged in a 100 mL autoclave without any tedious degassing operations, while 2 MPa of the N₂ was inserted. After the seal-up of the autoclave, the mixture was heated to 120 °C under the stirring allowing for the B–H coupling reaction for 5 h. The reactor was then cooled to room temperature, and the products were washed by 100 ml THF, CHCl₃, ethanol and hot water, respectively, and dried in a vacuum oven at 70 °C for 24 h.

S1.6 Characterization

The infrared characteristic peaks were tested by a Nicolet-iS50 Fourier-transform infrared (FTIR) spectrometer with the range of 4000–400 cm⁻¹. The solid-state ¹³C cross-polarization magic angle spinning nuclear magnetic resonance (SS ¹³C CP/MAS NMR) spectra were conducted on a Varian VNMRs-600 spectrometer. The thermogravimetric analysis (TGA) was measured by a thermal Gravimetric Analyzer PerkinElmer TGA-7 America at a heating speed of 10 °C min⁻¹. N₂ adsorption/desorption isotherms, CO₂ adsorption and H₂ adsorption isotherm studies were performed on a

Micromeritics ASAP 2020 HD88 after the sample degassing under a high vacuum at 120 °C for 5 hours. The Brunauer–Emmett–Teller (BET) equation was applied to calculate the surface area, while the pore size distribution (PSD) and pore volume (PV) were calculated based on the non-local density functional theory (NLDFT). The adsorption heats of CO₂ were calculated using the package in the Micromeritics ASAP 2020 HD88 based on the adsorption data conducted at 273 K and 298 K. Surface morphology of samples was observed by a field scanning electron microscopy (SEM) using a FEI Nova NanoSEM 230. Solid-state ultraviolet-visible near-infrared (UV-vis/NIR) spectra were recorded on an Agilent Cary 7000. Concentrations of heavy metal ion were obtained through an inductive coupled plasma emission spectrometer (ICP) of Shimadzu ICPE-9000.

S1.7 Mercury ion adsorption experiment

Mercury ion solution, which was the main pollutant in the wastewater from the polyvinyl chloride (PVC) industrials, was prepared by the HgCl₂ and deionized water. The dose of all adsorption experiments was fixed at 1 g L⁻¹ (with 10 mg of the adsorbent in 10 mL of the heavy metal solution). During the adsorption process, the oscillation speed was kept at 200 rpm, and the solution after treatment was collected using a filtration *via*. a syringe filter (0.45 μm membrane filter) for the ICP test. The maximum adsorption capacity towards the mercury ions was acquired in the mercury ion solution with an initial concentration of 1200 mg L⁻¹ without a pH adjustment (the pH was around 6), and the samples with the best adsorption capacity were selected for more detailed adsorption kinetic, isotherm and thermodynamics investigations. In the kinetic experiment, mercury ion solutions with differential initial concentration of 50 mg L⁻¹, 200 mg L⁻¹ or 400 mg L⁻¹ were used to estimate the adsorption rate of the porosity improved PTPA under different contact times (0-180 min) at 298 K. In the isotherm study, the FZU-PTPA was mixed with mercury ion solutions with differential initial concentrations for 5 h. In the adsorption selectivity study, PTPA was added to a mixed solution containing HgCl₂, Cu(NO₃)₂, Zn(NO₃)₂, La(NO₃)₂, Pb(NO₃)₂, Co(NO₃)₂, Ni(NO₃)₂ with 200 mg L⁻¹ for each to investigate the adsorption selectivity and applicability towards Hg(II) of our samples in the practical application.

S1.8 Methodology

S1.8.1 Kinetic study

In kinetic study, pseudo-first-order kinetic model and pseudo-second-order kinetic model were adopted to extract the adsorption kinetic parameters of mercury ions on PTPA. The mercury ions transfer situation and rate control steps in the physical and chemical reaction could be conducted by model fitting. For each model, the linear and nonlinear fitting methods were used. The formulas used are as follows,

pseudo-first-order kinetic model

$$\frac{dQ_t}{dt} = k_1 \ln(Q_e - Q_t) \quad (\text{nonlinear, S1}),$$

$$Q_t = Q_e(1 - e^{-k_1 t}) \quad (\text{linear, S2}),$$

where the k_1 is rate constant for pseudo-first-order kinetic model, and Q_e (mg g⁻¹) and Q_t (mg g⁻¹) are the absorption capacity of equilibrium and at time t (min), respectively.

pseudo-second-order kinetic model

$$\frac{dQ_t}{dt} = k_1 \ln(Q_e - Q_t)^2 \quad (\text{nonlinear, S3}),$$

$$Q_t = \frac{k_2 Q_e^2 t}{1 + k_2 Q_e t} \quad (\text{linear, S4}),$$

where the k_2 (g mg⁻¹ min) is rate constant for pseudo-second-order kinetic model, and Q_e (mg g⁻¹) and Q_t (mg g⁻¹) are the absorption capacity of equilibrium and at time t (min), respectively.

S1.8.2 Isotherm study

As for isotherm, the mercury ion adsorption capacity could be evaluated by the Freundlich model and Langmuir model with linear and nonlinear fitting. Freundlich model is an empirical formula based on hypothesis that adsorbents can be adsorbed at multiple sites, while the Langmuir model is based on a monolayer adsorption theory.

Freundlich model

$$Q_e = K_F C_e^{\frac{1}{n}} \quad (\text{nonlinear, S5}),$$

$$\ln Q_e = \ln K_F + \frac{1}{n} \ln C_e \quad (\text{linear, S6}),$$

where the Q_e (mg g⁻¹) and C_e (mg L⁻¹) are the absorption capacity and concentration at equilibrium, respectively, and K_F stands for the Freundlich constant;

Langmuir model

$$Q_e = Q_{max} \frac{K_L C_e}{1 + K_L C_e} \quad (\text{nonlinear, S7}),$$

$$\frac{C_e}{Q_e} = \frac{1}{Q_{max}} C_e + \frac{1}{K_L Q_{max}} \quad (\text{linear, S8}),$$

where the Q_e (mg g⁻¹) and C_e (mg L⁻¹) are the absorption capacity and concentration at equilibrium, respectively, and K_L stands for the Langmuir constant.

S1.8.3 Thermodynamic study

The adsorption thermodynamic model was adopted to describe the spontaneity of the adsorption process, the disorder degree of system and the temperature influence on adsorption. The Van Hoff equation describing thermodynamics is as follows,

$$K_D = \frac{C_{A,e}}{C_e} \quad (\text{S9}),$$

$$\Delta G = -RT \ln K_D \quad (\text{S10}),$$

$$\ln K_D = \frac{\Delta S}{R} - \frac{\Delta H}{RT} \quad (\text{S11}),$$

where K_D is the distribution coefficient, where the $C_{A,e}$ and C_e refer to the concentration of adsorbed and solution when adsorption reach equilibrium, respectively; T is for temperature (K) and R is the gas constant could be calculated as 8.314(J mol⁻¹ K⁻¹). While the ΔG (kJ mol⁻¹), ΔS (J mol⁻¹ K⁻¹) and ΔH (kJ mol⁻¹) refer to Gibbs free energy change, entropy change and enthalpy change as usual.

S1.9 DFT calculation

The structural optimization of FZU-PTPA and the interaction between the FZU-PTPA and mercury ions were calculated by a Gaussian 16 W software. The basis set of b3pw91/6-31g(d) was used for the structural optimizing of FZU-PTPA, and the calculation for the interaction between FZU-PTPA and mercury ions was performed with the GeneECP basis set (b3pw91 for FZU-PTPA and SDD for mercury ion). All calculations were performed on a water-based solvation model.

S2 Results and discussion

S2.1 Successful coupling of 1,4-dichlorobenzene and tri(4-aminophenyl) amine

The successful coupling of the 1,4-dichlorobenzene and tri(4-aminophenyl) amine, even reacted in a very short 5 h time period, could be also verified by the FTIR investigation in Figure 3(b), which showed the characteristic peaks assigned to the core tri(4-aminophenyl)amine and linker 1,4-dichlorobenzene, but showed the absence of peaks assigned to C-Cl in the 1,4-dichlorobenzene (situated at around 1004 and 1070 cm^{-1} , shown in a purple strip) and the extensive reduce of peaks ascribed to $-\text{NH}_2$ in the tri(4-aminophenyl) amine (situated at around 3400 and 3300 cm^{-1} , shown in a yellow strip).

S2.2 Doping in the PTPA-Cl

The PTPA-Cl was doped by the Cl^- , which could be confirmed by the SS ^{13}C NMR spectra, FTIR and XPS shown in Figure 3 (b-d). Specifically, an additional peak at 1146 cm^{-1} and a significant broadening of the quinoid amine peak at 1580 cm^{-1} highlighted in green strips could be observed in the FTIR spectrum compared to that of the FZU-PTPA, first suggesting some degree of electron delocalization and the doping on the quinoid amine on the PTPA-Cl chain. Additionally, a clear new peak assigned to the positively charged N ($-\text{N}^{+-}$) at 401.4 eV arose in the XPS N1s spectra, again revealing the doping state of the PTPA-Cl. This doping caused a slight response in the SS ^{13}C NMR at a chemical shift of ca. 119.9 ppm (in a green strip in the Figure 3(b)), which was another indicator for the doped PTPA-Cl. We reasoned the doping fact was caused by the by-product HCl during the reaction; the Cl^- with a smaller radius than Br^- would be easier to be doped onto the PTPA-Cl.^{1,2}

S2.3 Detection of the $-\text{NH}_2$ from the XPS results

We could also observe a new species of $-\text{NH}_2$ in the XPS N1s spectra, which also caused a small new peak in the FTIR spectrum at ca. 3400 cm^{-1} , indicating the presence of the unreacted amine group from the core in the PTPA-Cl. This may be caused by the relatively inert 1,4-dichlorobenzene that could not fully consume the amine during the coupling.

S2.4 Confirming the synthetic mechanism of the FZU approach from the Hansen-solubility-parameter point of view

The influence of solvents with differential Hansen solubility parameters (HSP, δ_T) on the over-heating temperature also support the mechanism very well. It could be seen from Figure S21 and Table 1, the specific surface area of PTPA synthesized in the toluene was lower than that in THF when presented in the same reaction temperature, while its over-heating temperature was higher than that in THF. According to the HSP theory, the solvent with the larger difference in δ_T between the solvent and polymer would result in less compatibility for the polymer polymerization, thus an earlier stage of the phase separation during the polymerization and a poorer porosity for the polymer would be occurred. As we calculated, the toluene with δ_T of 18.2 was more incompatible for PTPA polymerization (with δ_T of 22.6) compared to THF with δ_T of 19.5 ($|\delta_{T, \text{Toluene}} - \delta_{T, \text{PTPA}}| = 4.4$ vs. $|\delta_{T, \text{THF}} - \delta_{T, \text{PTPA}}| = 3.1$).³ Consistently, for a richer porosity, higher reaction temperature should be applied to ensure a more effective polymerization before the easier phase separation when in the toluene compared to that in THF.

S3 Supplementary Figures

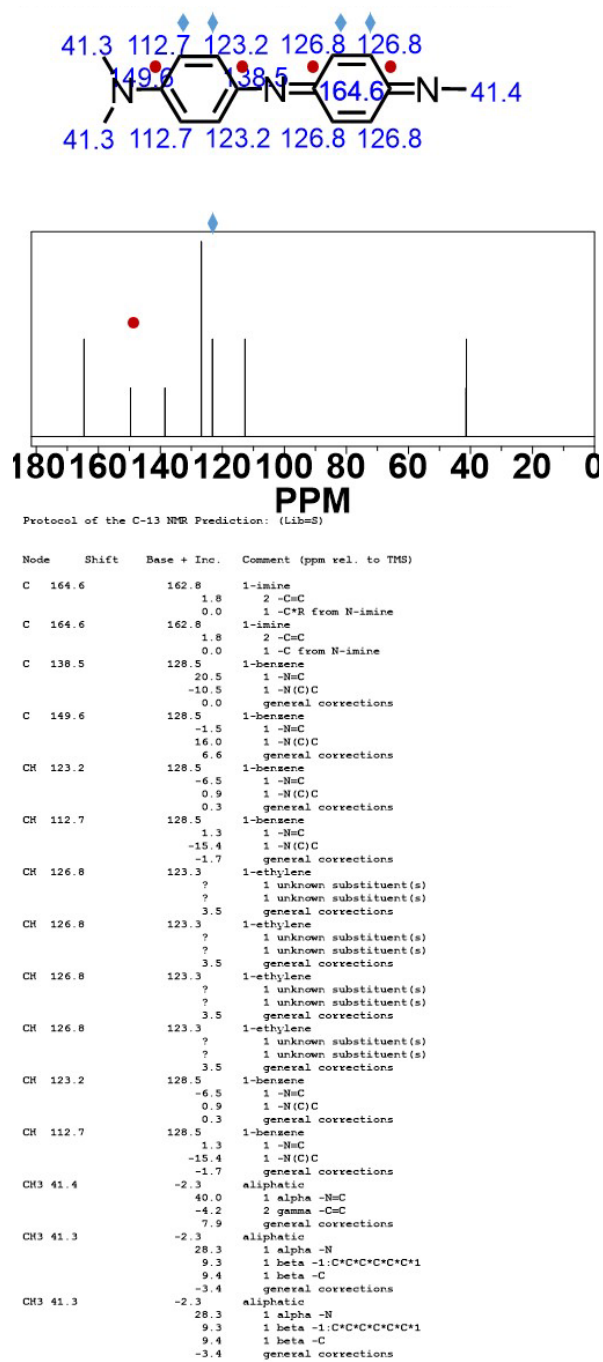


Figure S1 Calculated ¹³C NMR spectrum of the PTPA oligomer through the ChemDraw software package

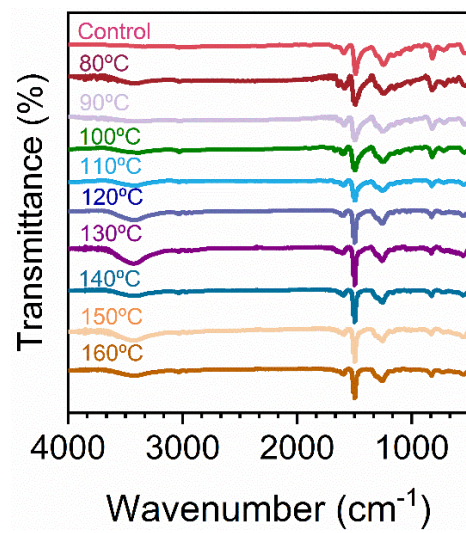


Figure S2 FTIR spectra of FZU-PTPA synthesized under differential reaction temperature

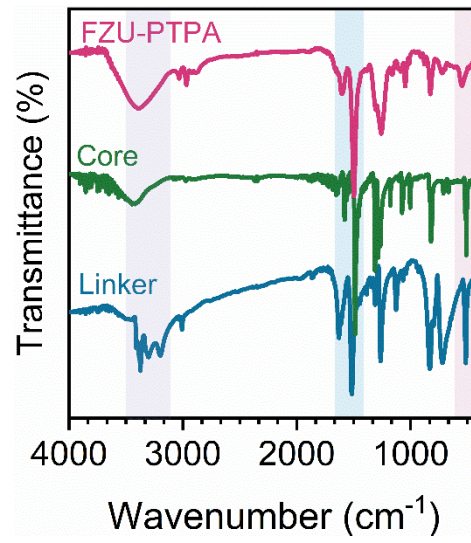


Figure S3 FTIR spectra of FZU-PTPA, core (tri(4-bromophenyl) amine) and linker (phenylenediamine)

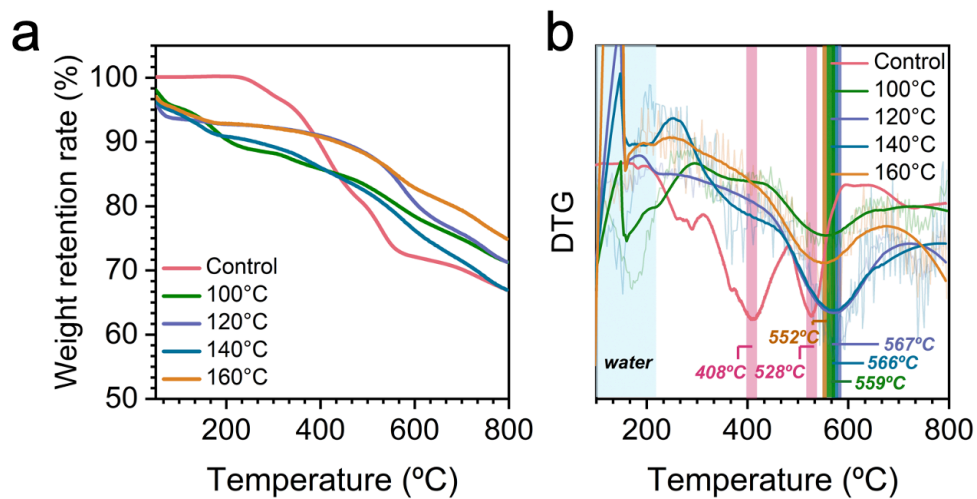


Figure S4 TGA (a) and the corresponding DTGA (b) curves of the FTIR spectra of FZU-PTPA synthesized under differential reaction temperature

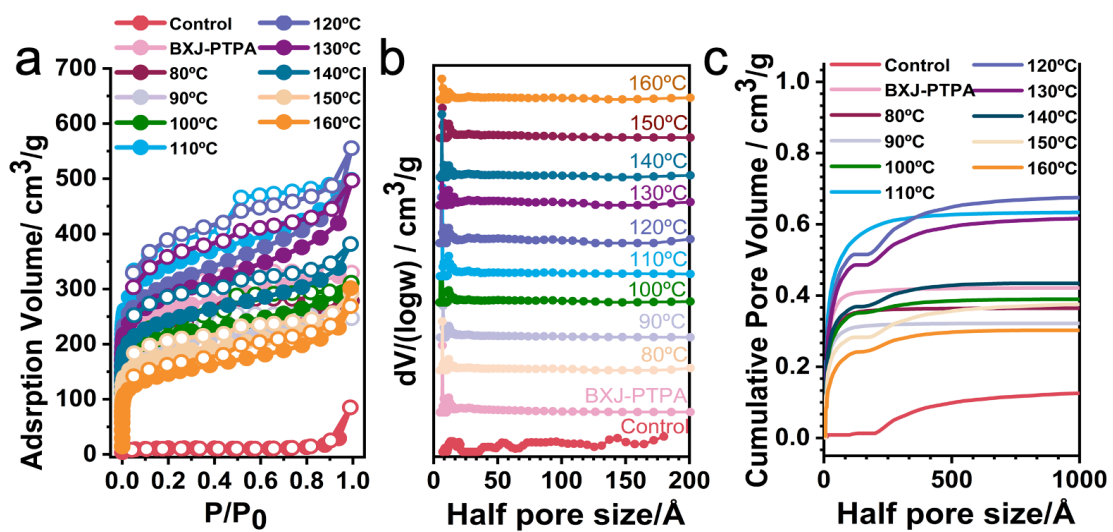


Figure S5 N₂ adsorption isotherm (a), pore size distribution (PSD, b) and pore volume distribution (PV, c) of FZU-PTPA synthesized under differential temperature

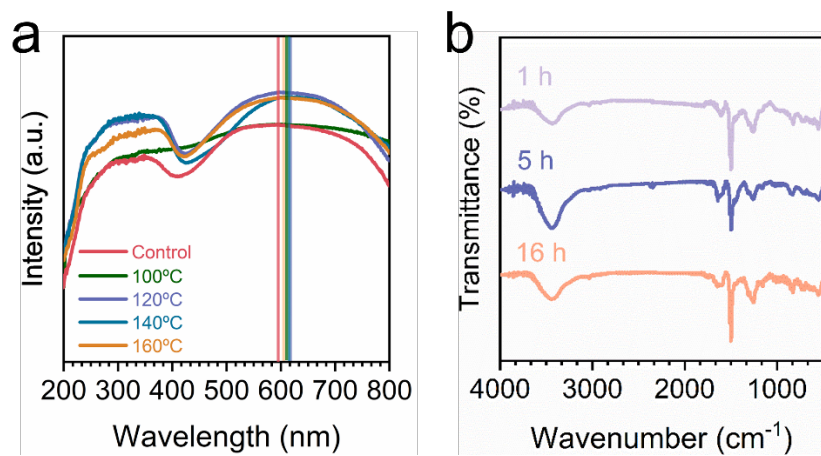


Figure S6 (a)SS UV/Vis NIR spectra of FZU-PTPA under differential reaction temperature; (b)FTIR spectra of FZU-PTPA synthesized under differential reaction time

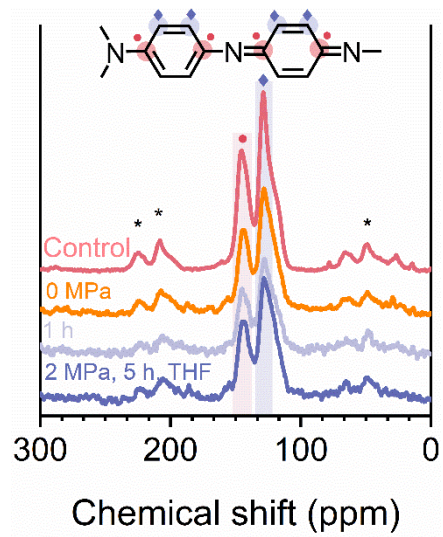


Figure S7 SS ¹³C NMR spectra of FZU-PTPA synthesized under differential reaction time and pressure

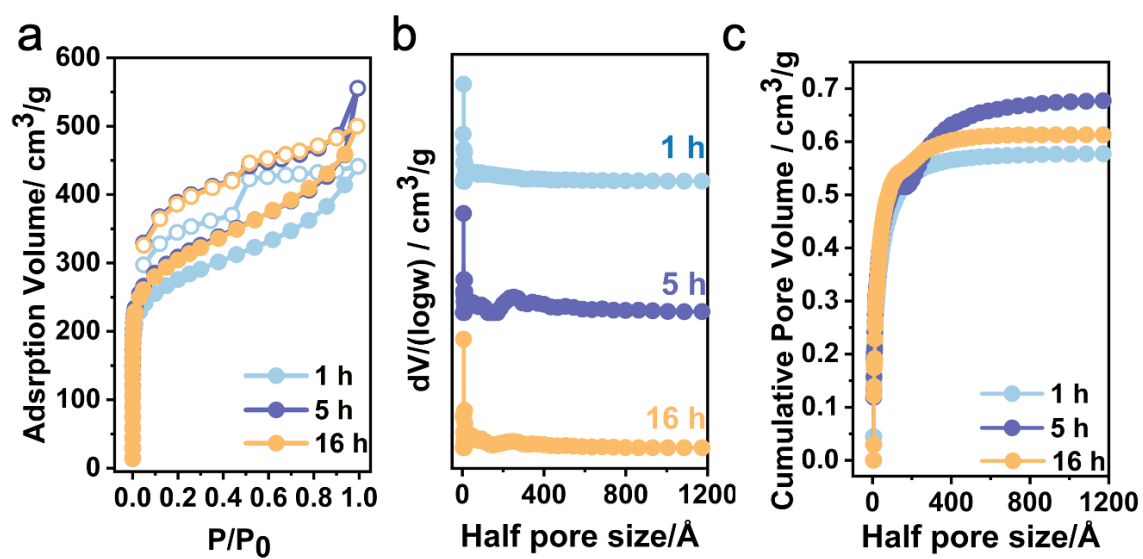


Figure S8 N₂ adsorption isotherm (a), pore size distribution (PSD, b) and pore volume distribution (PV, c) of FZU-PTPA synthesized under differential reaction time

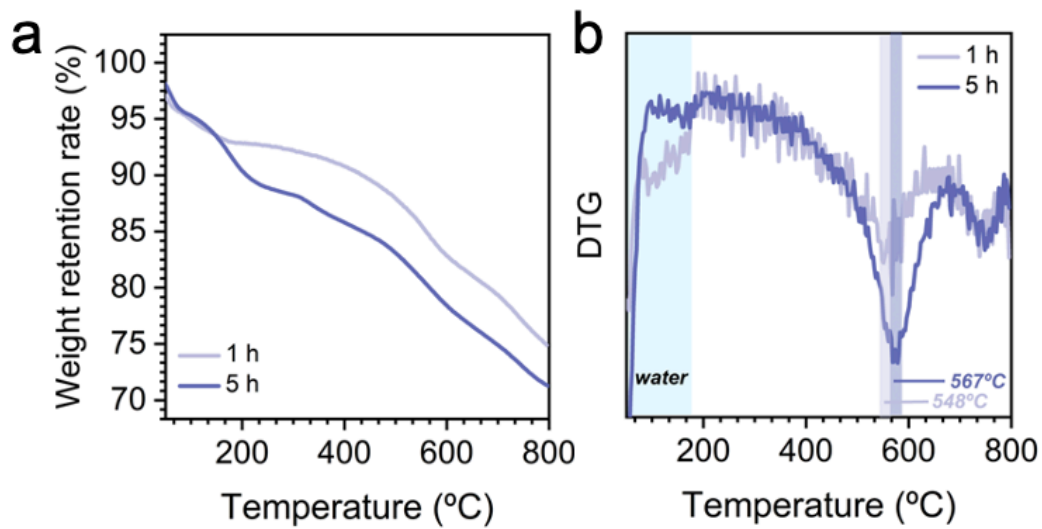


Figure S9 TGA (a) and the corresponding DTG (b) curves of the FTIR spectra of FZU-PTPA synthesized under differential reaction time

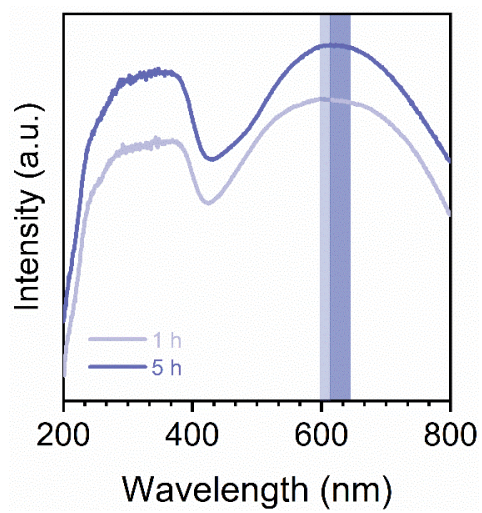


Figure S10 SS UV/Vis NIR of FZU-PTPA synthesized under differential reaction time

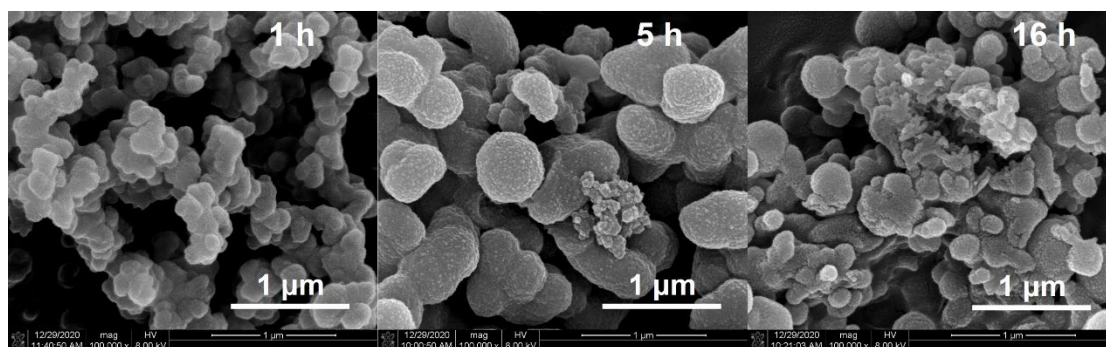


Figure S11 SEM images of FZU-PTPA synthesized under differential reaction time

The sphere grew with the reaction time from 1 h to 5 h, but slightly decomposed after 16 h synthesis, with no porosity changed (Table 1). We reasoned that for this approach, 5 h was enough for the reaction to finish, and a further reaction, under a strong stirring, would break the sphere physically. As such, broken spheres could be seen in the SEM images of FZU-PTPA with 16 h reaction, with approaching porosity to the sample synthesized within 5 h.

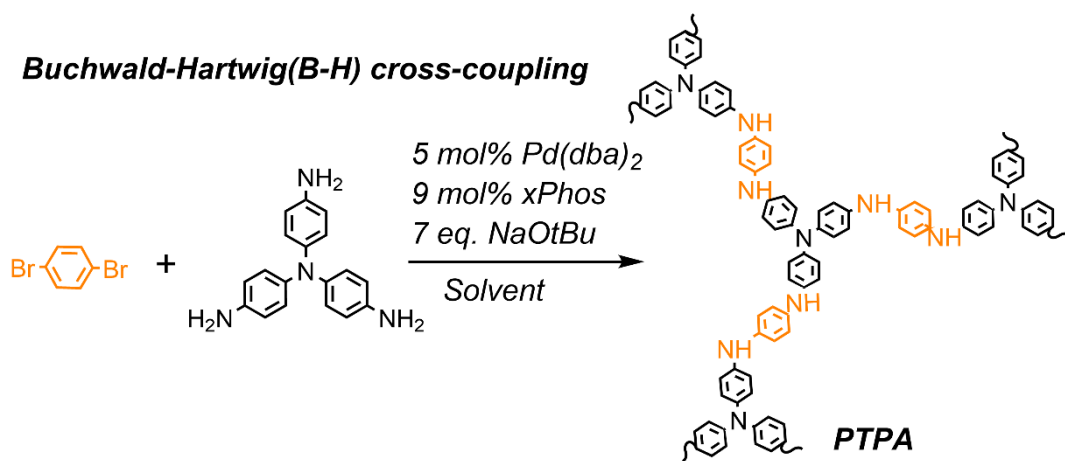


Figure S12 Synthesis of PTPA via Buchwald–Hartwig cross-coupling of 1,4-dibromobenzene and tris(4-aminophenyl)amine.

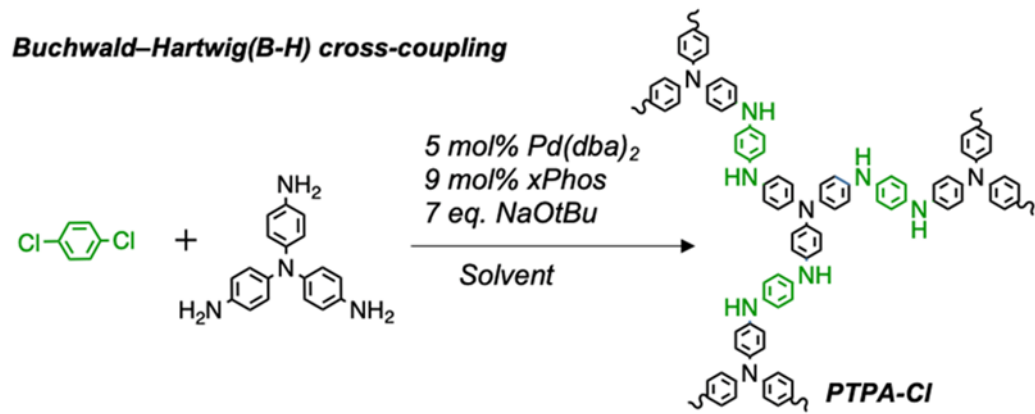


Figure S13 Synthesis of PTPA-Cl via Buchwald–Hartwig cross-coupling of 1,4-dichlorobenzene and tris(4-aminophenyl)amine.

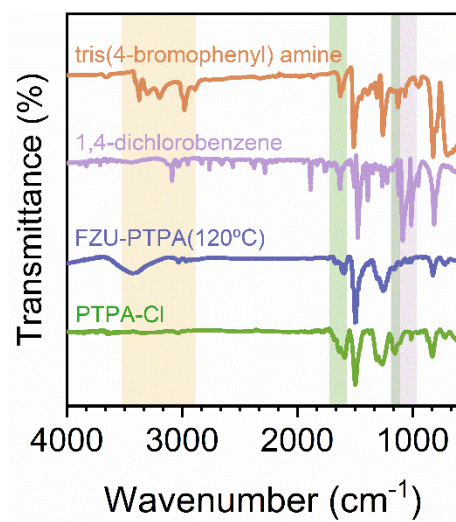


Figure S14 FTIR spectra of FZU-PTPA (120 °C) and PTPA-Cl.

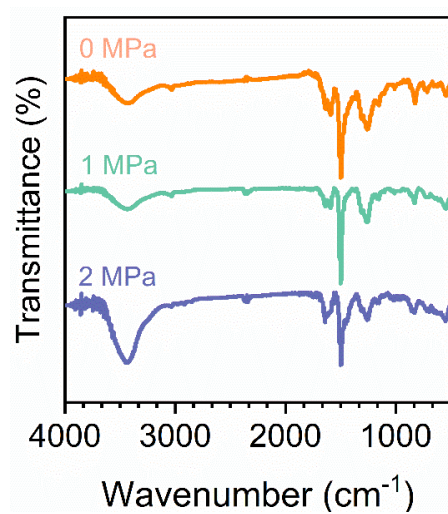


Figure S15 FTIR spectra of FZU-PTPA synthesized under differential pressure of inserted N₂

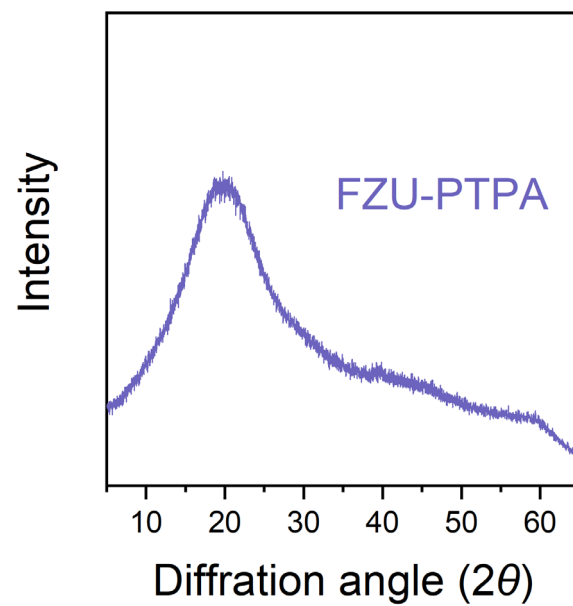


Figure S16 XRD spectra of FZU-PTPA (120 °C)

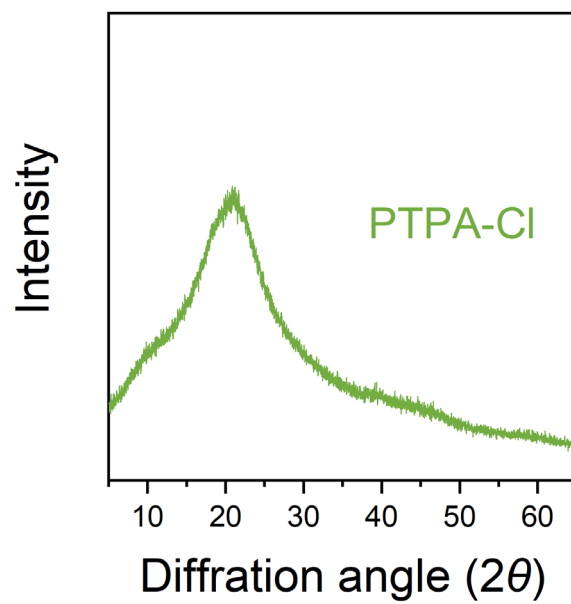


Figure S17 XRD spectra of PTPA-Cl (120 °C)

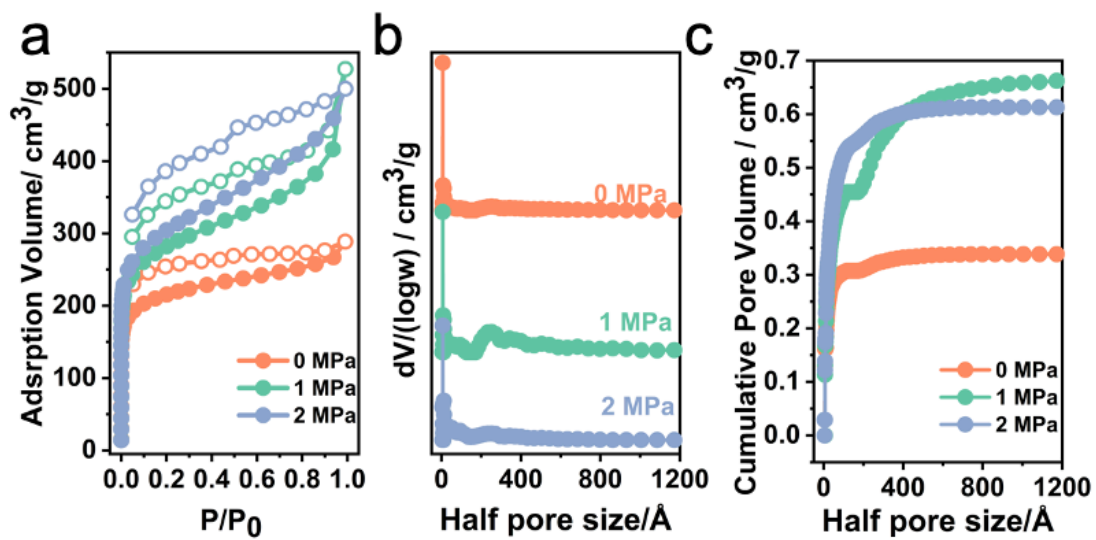


Figure S18 N₂ adsorption isotherm (a), pore size distribution (PSD, b) and pore volume distribution (PV, c) of FZU-PTPA synthesized under differential pressure of inserted N₂

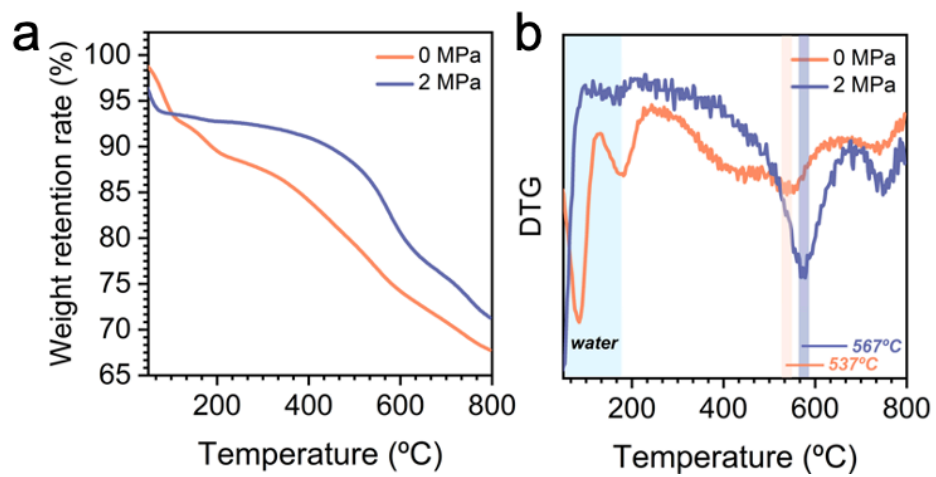


Figure S19 TGA (a) and DTGA (b) curves of FZU-PTPA synthesized under differential pressure of inserted N₂

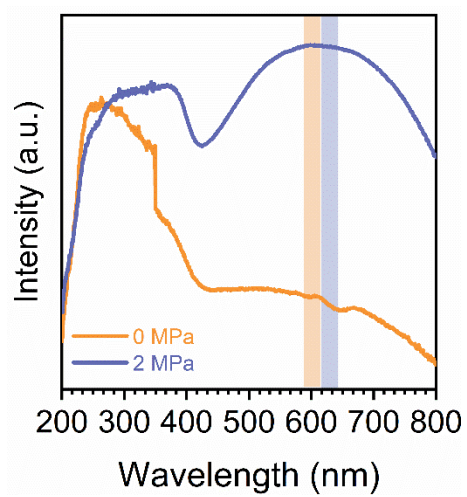


Figure S20 SS UV/Vis spectra of FZU-PTPA synthesized under differential pressure of inserted N₂

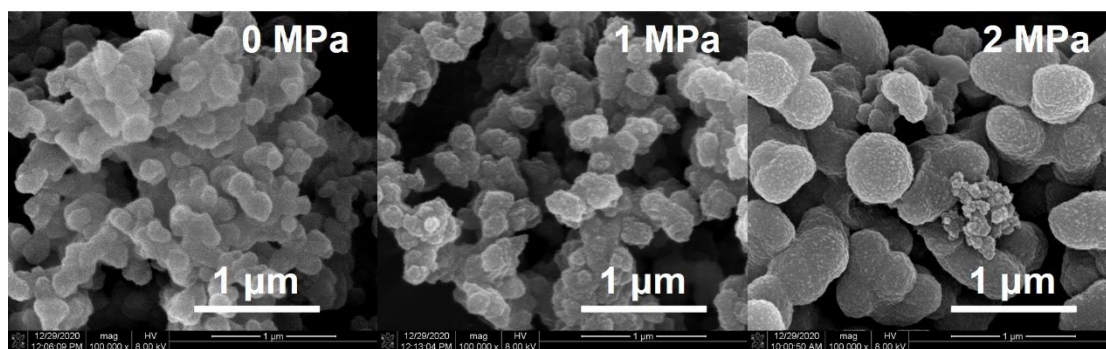


Figure S21 SEM images of FZU-PTPA synthesized under differential pressure of inserted N₂

The presence of O₂ would impede the growth of polymers during the polymerization through influencing the Pd-catalysis efficiency, resulting in smaller radius of sphere compared to that of the samples synthesized with lower partial pressure of O₂ (for example, samples produced under additional 2 MPa of N₂).

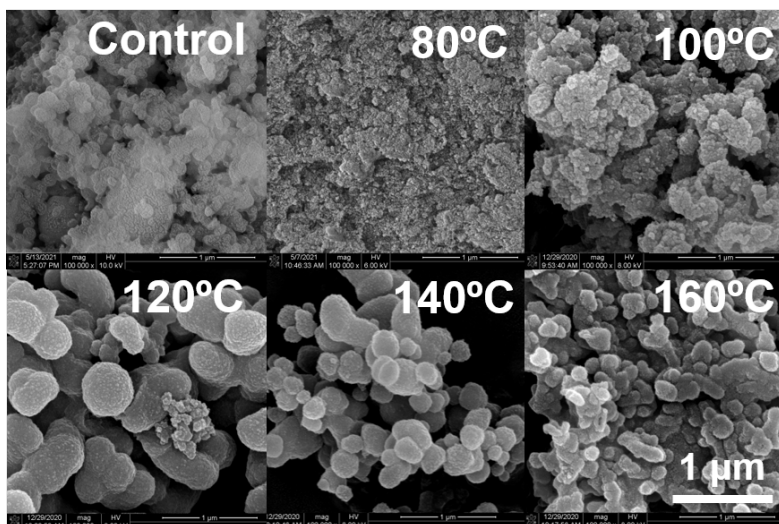


Figure S22 SEM images of FZU-PTPA synthesized under differential reaction temperatures

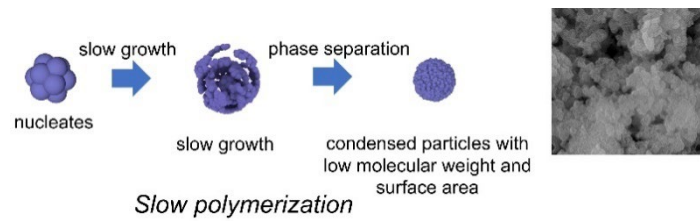


Figure S23 illustration of the nucleate growth of PTPA synthesized in a poor polymerization process (for example, the process by using the conventional polymerization method) ⁴⁻⁶

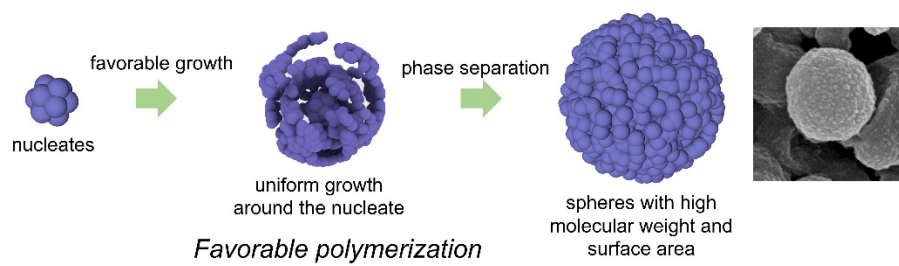


Figure S24 illustration of the nucleate growth of PTPA synthesized in a favorable polymerization process (for example, the process by using the FZU polymerization method under a mild temperature) ⁴⁻⁶

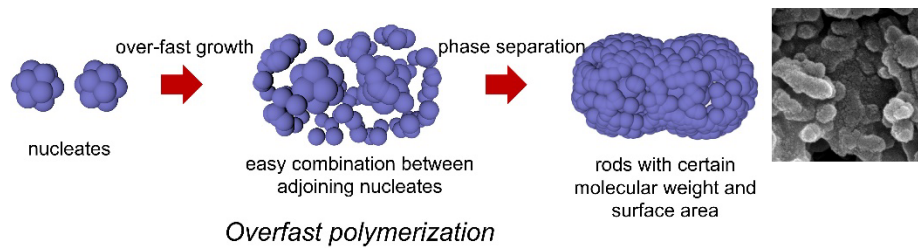


Figure S25 illustration of the nucleate growth of PTPA synthesized in an over-fast polymerization process (for example, the process by using the FZU polymerization method under an over-high temperature) ⁴⁻⁶

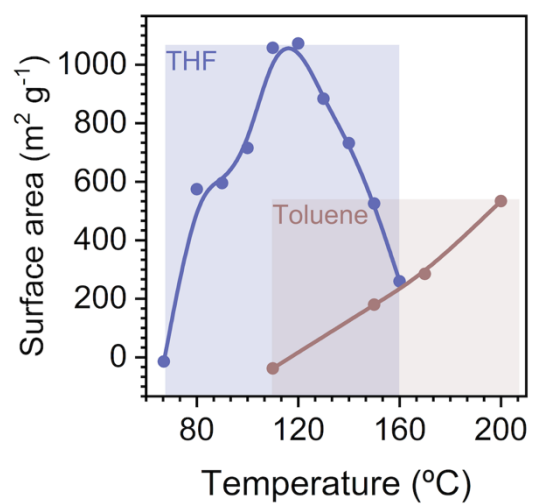


Figure S26 the relationship between the reaction temperature and the specific surface area of PTPAs synthesis in different solvent

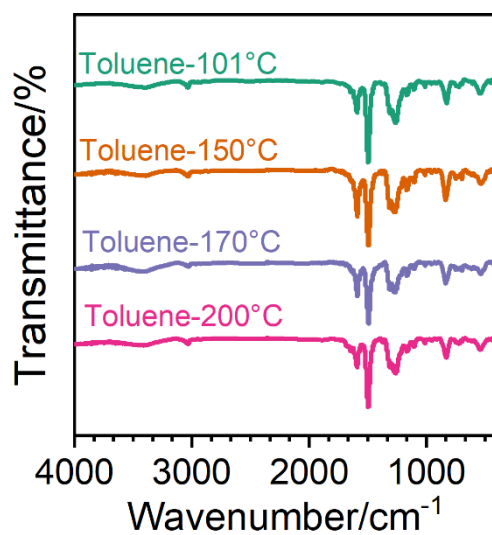


Figure S27 FTIR spectra of FZU-PTPA synthesized in toluene under differential temperature

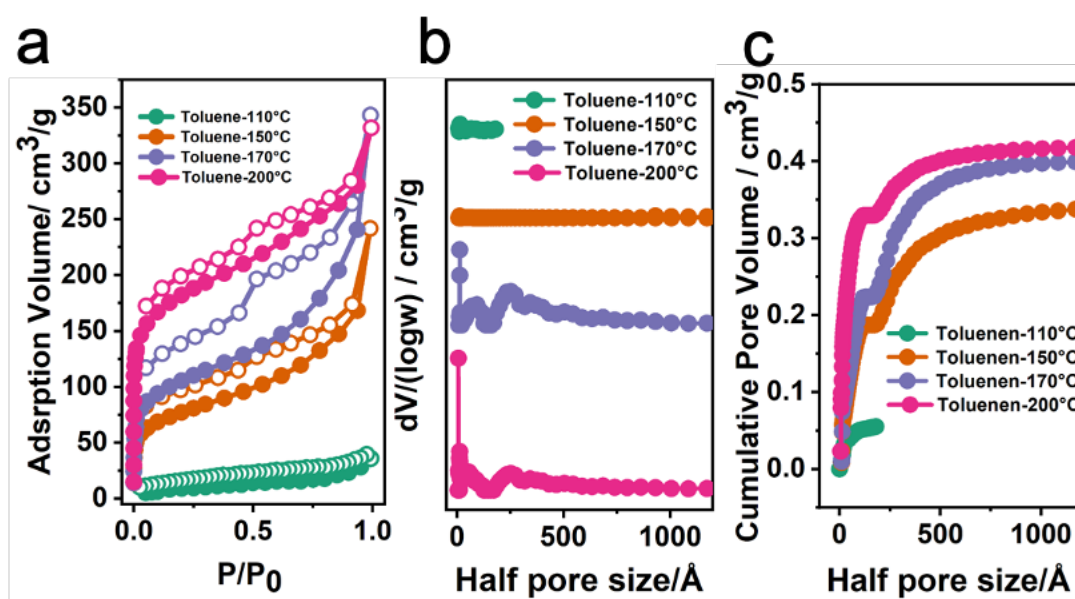


Figure S28 N_2 adsorption isotherm (a), pore size distribution (PSD, b) and pore volume distribution (PV, c) of FZU-PTPA synthesized in toluene under differential temperature

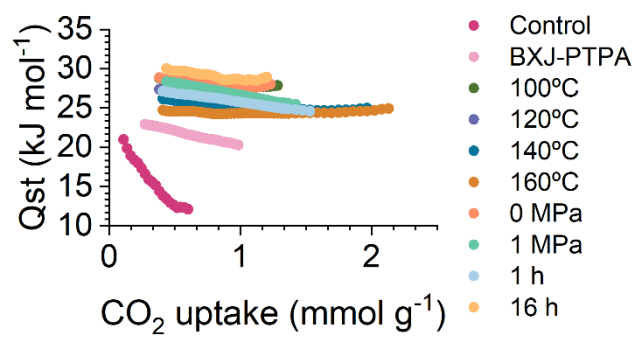


Figure S29 isosteric heat of adsorption (Q_{st}) of FZU-PTPA acquired in the Micromeritics ASAP 2020 HD88 based on the adsorption data conducted at 273 K and 298 K

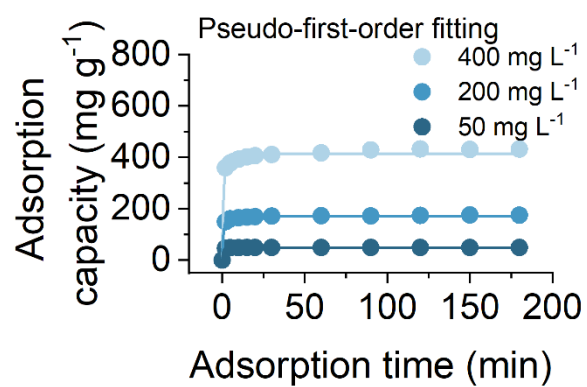


Figure S30 fitting of kinetic data with the pseudo-first-order model of FZU-PTPA

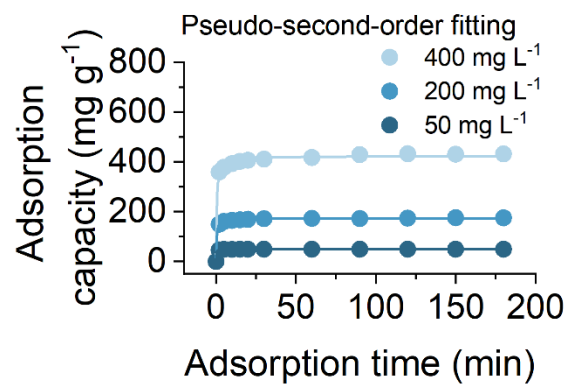


Figure S31 fitting of kinetic data with the pseudo-second-order model of FZU-PTPA

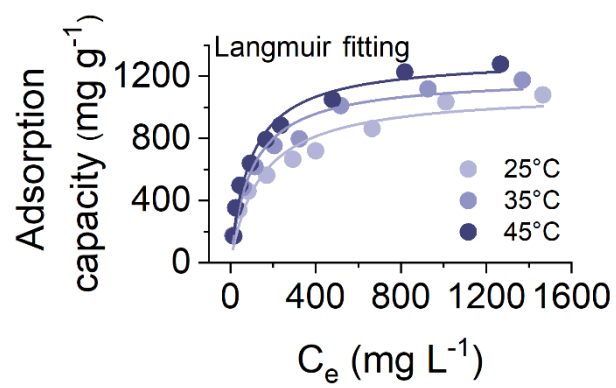


Figure S32 fitting of isotherm data with the Langmuir model of FZU-PTPA

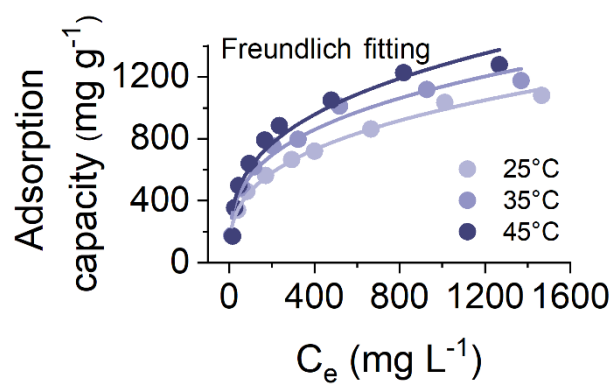


Figure S33 fitting of isotherm data with the Freundlich model of FZU-PTPA

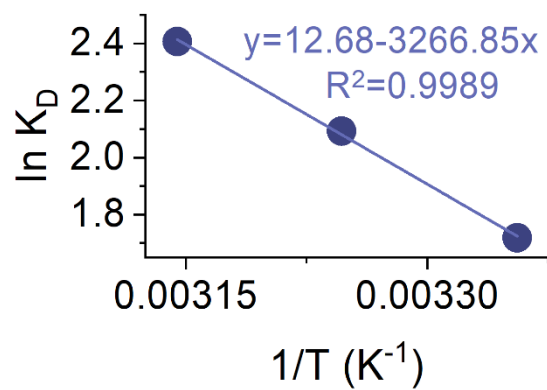


Figure S34 fitting of thermodynamic data of FZU-PTPA

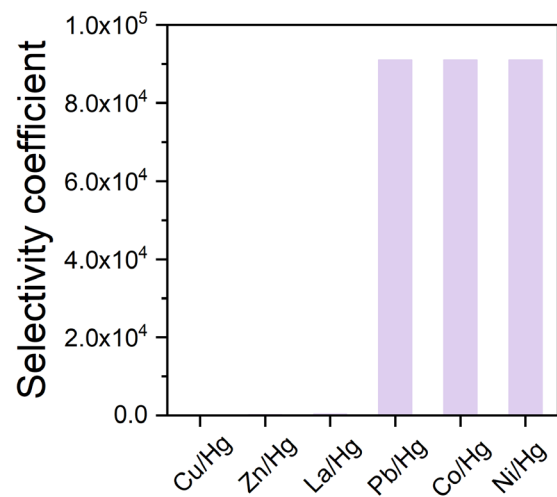


Figure S35 Selectivity coefficients of Hg(II) against other cations obtained from the batch adsorption experiments

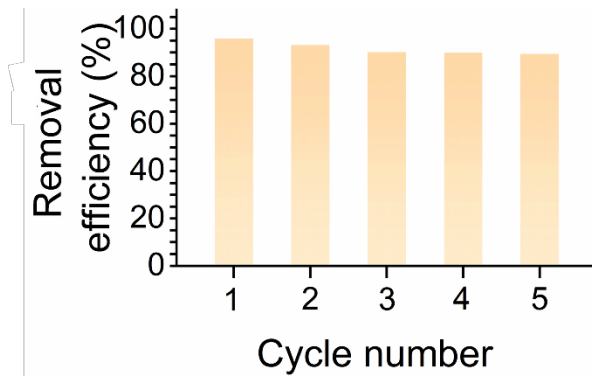


Figure S36 The Hg(II) removal efficiency of our FZU-PTPA in a 5-cycles reuse

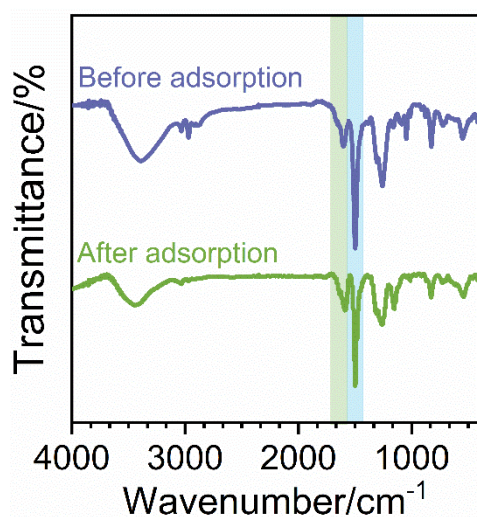


Figure S37 FTIR spectra of FZU-PTPA (120 °C) before and after mercury adsorption

The intensity of the peak assigned to the benzenoid amine ($-\text{NH}-$) situated at 1480 cm^{-1} (highlighted in blue) reduced, while that of the peak assigned to the quinoid amine ($-\text{N}=\text{}$) situated at 1590 cm^{-1} (highlighted in green) increased after mercury adsorption, indicating a consumption of $-\text{NH}-$ by the mercury during the adsorption and the corresponding production of $-\text{N}=\text{}$.

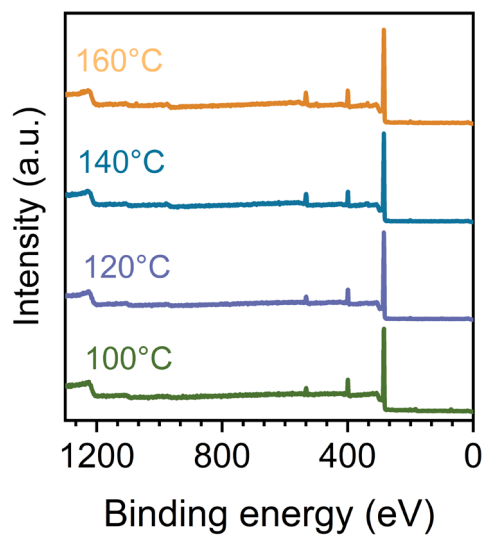


Figure S38 full-scan XPS spectra of FZU-PTPA synthesized under different temperature

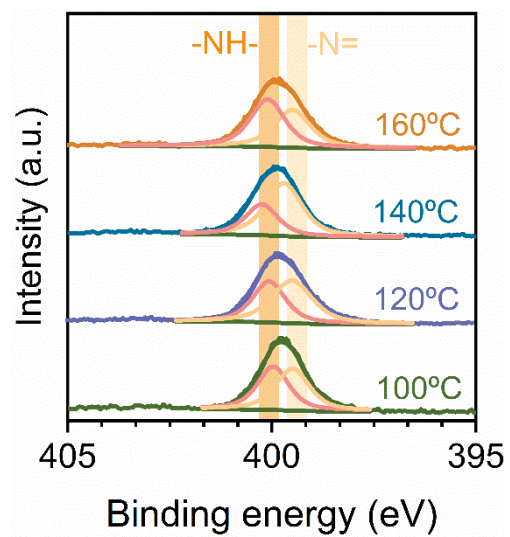


Figure S39 N1s XPS spectra of FZU-PTPA synthesized under different temperature

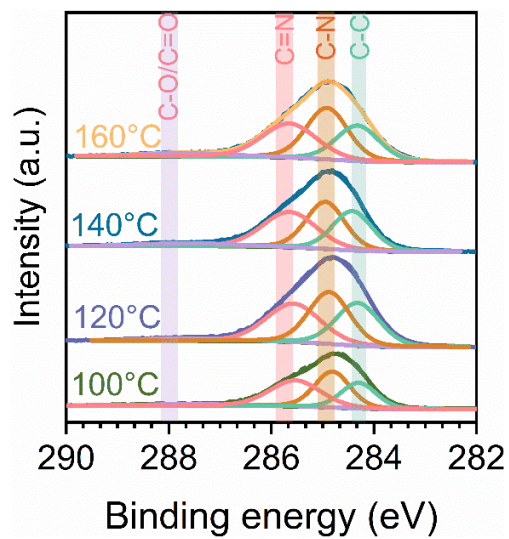


Figure S40 C1s XPS spectra of FZU-PTPA synthesized under different temperature

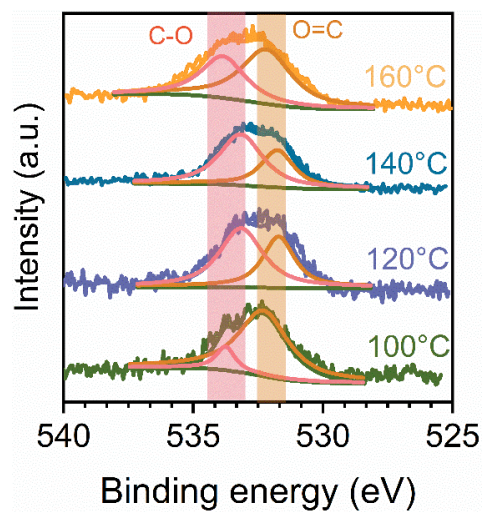


Figure S41 O1s XPS spectra of FZU-PTPA synthesized under different temperature

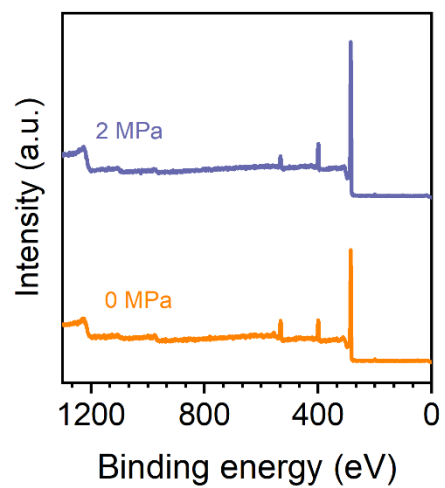


Figure S42 full-scan XPS spectra of FZU-PTPA synthesized under different pressure

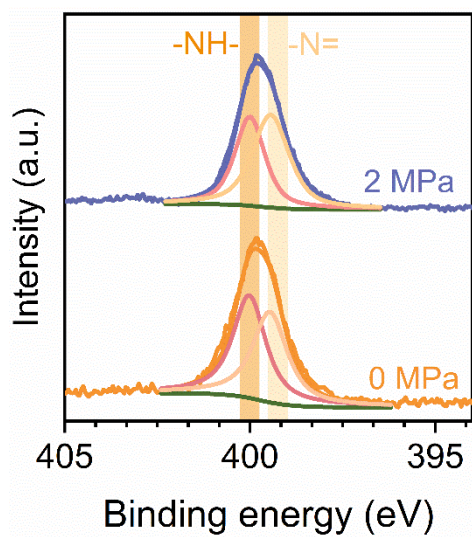


Figure S43 N 1s XPS spectra of FZU-PTPA synthesized under different pressure

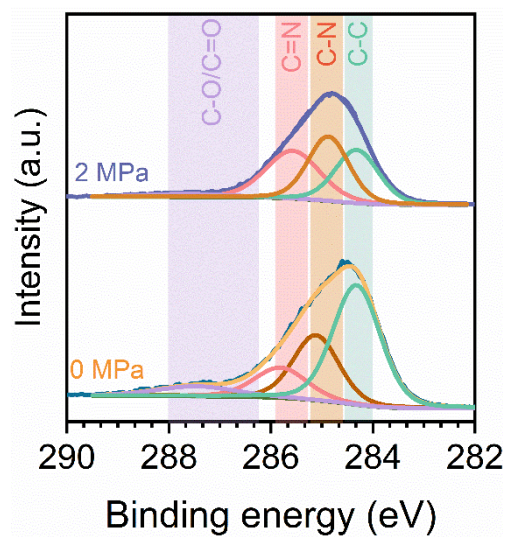


Figure S44 C 1s XPS spectra of FZU-PTPA synthesized under different pressure

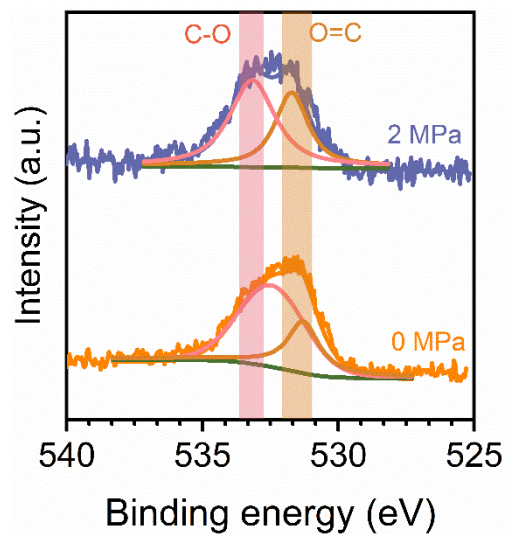


Figure S45 O 1s XPS spectra of FZU-PTPA synthesized under different pressure

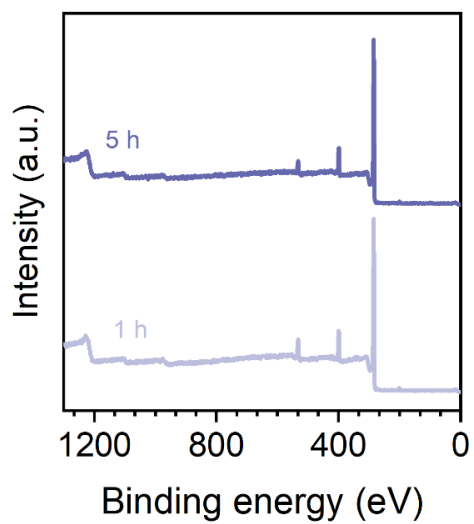


Figure S46 full-scan XPS spectra of FZU-PTPA synthesized under different reaction time

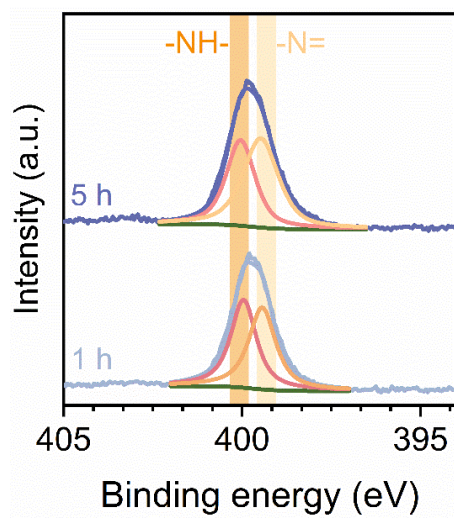


Figure S47 N 1s XPS spectra of FZU-PTPA synthesized under different reaction time

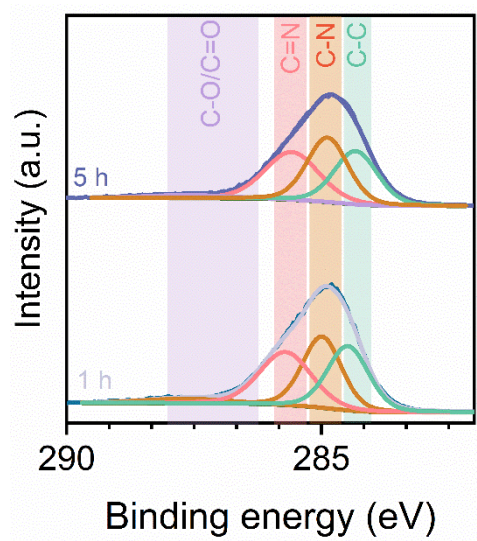


Figure S48 C 1s XPS spectra of FZU-PTPA synthesized under different reaction time

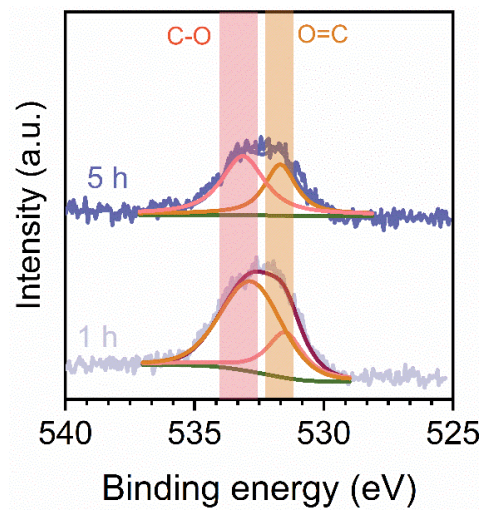


Figure S49 O 1s XPS spectra of FZU-PTPA synthesized under different reaction time

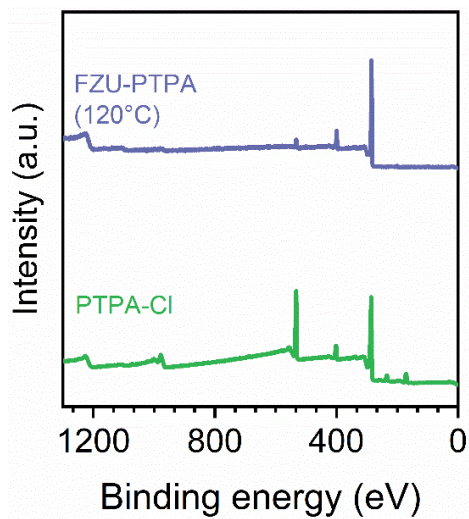


Figure S50 full-scan XPS spectra of FZU-PTPA (2 MPa, 120 °C, 5 h) and PTPA-Cl

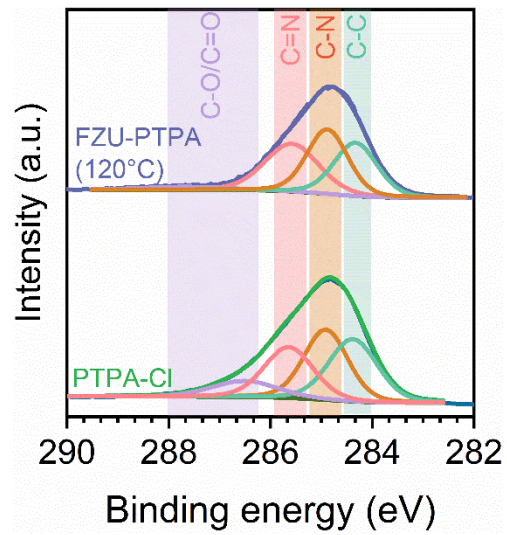


Figure S51 C 1s XPS spectra of FZU-PTPA (2 MPa, 120 °C, 5 h) and PTPA-Cl

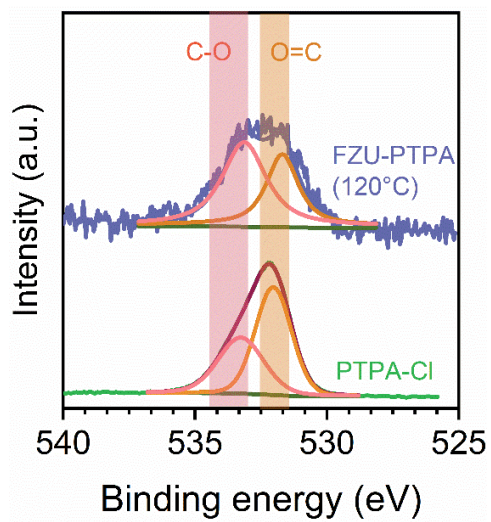


Figure S52 O 1s XPS spectra of FZU-PTPA (2 MPa, 120 °C, 5 h) and PTPA-Cl

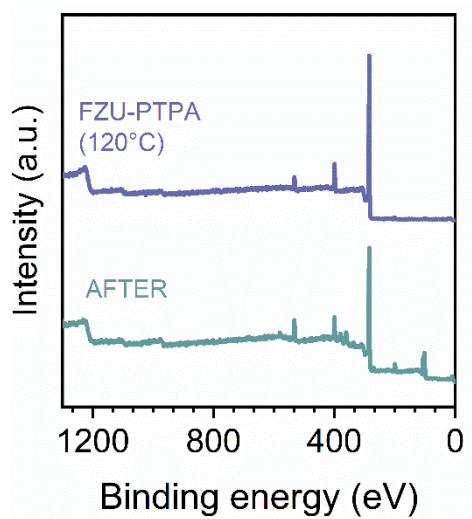


Figure S53 full-scan XPS spectra of FZU-PTPA before and after mercury adsorption

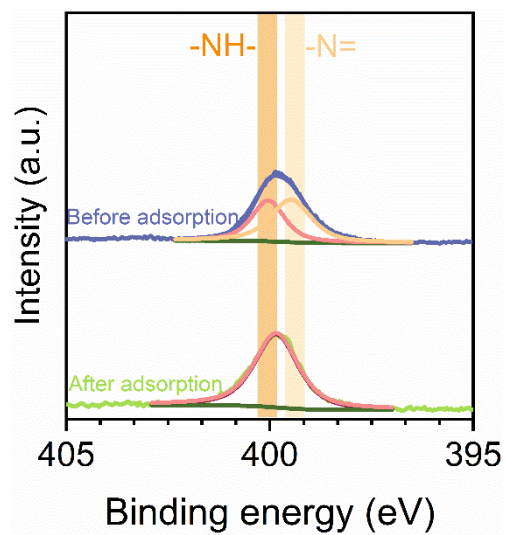


Figure S54 N1s XPS spectra of FZU-PTPA (120 °C) before and after mercury adsorption

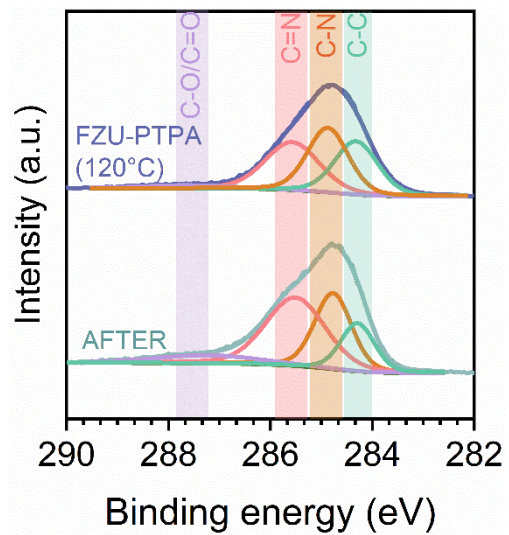


Figure S55 C1s XPS spectra of FZU-PTPA (120 °C) before and after mercury adsorption

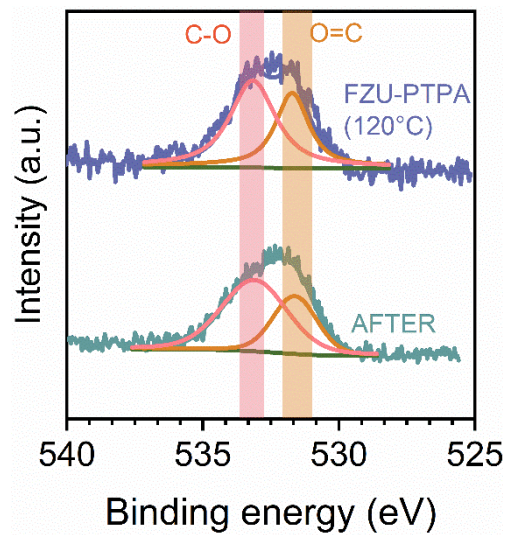


Figure S56 O1s XPS spectra of FZU-PTPA (120 °C) before and after mercury adsorption

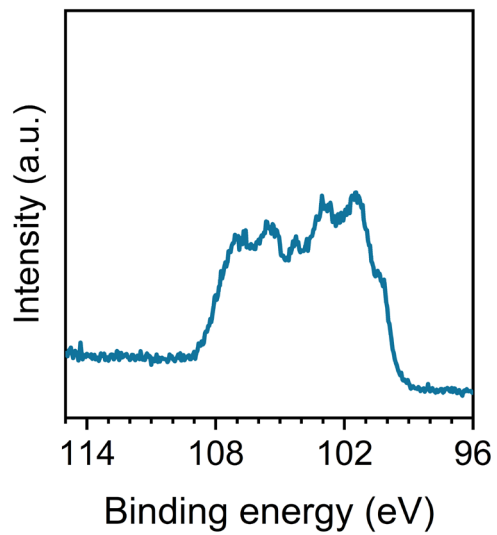


Figure S57 Hg 4d XPS spectra of FZU-PTPA (120 °C) after mercury adsorption

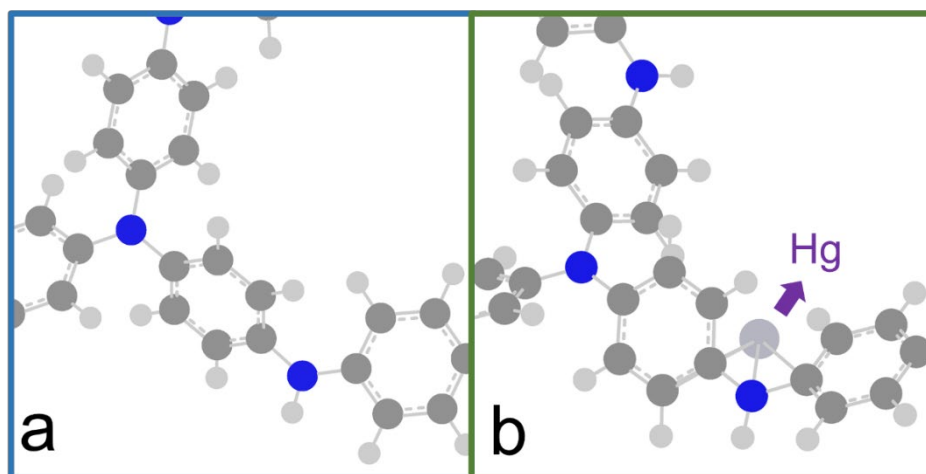


Figure S58 optimized structure of the oligomers of FZU-PTPA before (a) and after mercury adsorption (b) by Gaussian 16 W using a B3PW91/6-31g(d) basis set.

144	□	-0.16240
143	□	-0.16563
142	□	-0.16605
141	□	-0.16827
140	□	-0.16873
139	□	-0.16919
138	□	-0.17787
137	▣	-0.26350
136	▣	-0.29610
135	▣	-0.29638
134	▣	-0.32241
133	▣	-0.36009
132	▣	-0.36030
131	▣	-0.36732
130	▣	-0.36745
129	▣	-0.36848
128	▣	-0.36899
127	▣	-0.36929
126	▣	-0.37360
125	▣	-0.38365
124	▣	-0.41296
123	▣	-0.41311
122	▣	-0.42382
121	▣	-0.44821
120	▣	-0.44854
119	▣	-0.44999

Figure S59 Information of molecular orbital (in a unit of a.u.) of an oligomer of FZU-PTPA calculated by Gaussian 16 W using a B3PW91/6-31g(d) basis set.

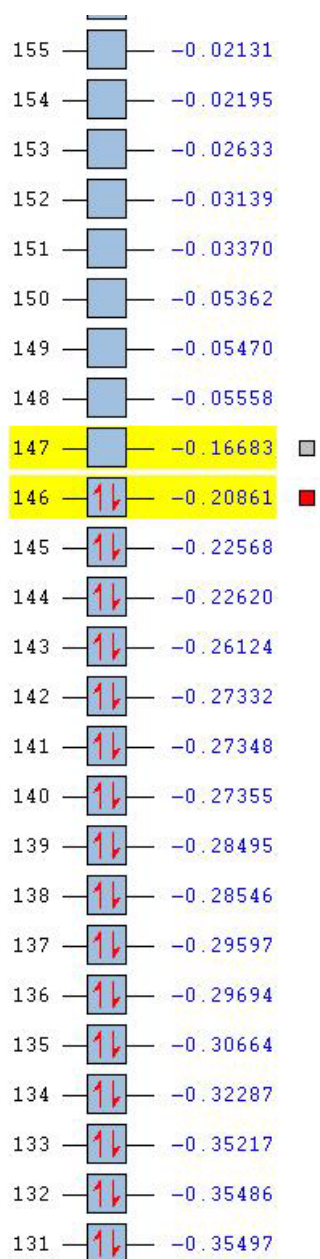


Figure S60 Information of molecular orbital (in a unit of a.u.) of an oligomer of FZU-PTPA after interaction with the mercury ions calculated by Gaussian 16 W using a B3PW91/6-31g(d) basis set.

S4 Supplementary tables

Table S1 peak positions and specific surface area of the SS UV/Vis spectra of FZU-PTPA

Sample	λ (nm)	Specific surface area ($\text{m}^2 \text{g}^{-1}$)
Control	595	58
100 °C	610	688
120 °C	620	1145
140 °C	615	804
160 °C	604	332

Table S2 CO₂ adsorption capacity of advanced porous materials

Adsorbent	Adsorption capacity (mmol g ⁻¹)	Adsorption capacity (wt%)	Ref.
FZU-PTPA	4.06 (1 bar)	17.86	this work
POM	3.73 (1 bar)	16.40	7
PCP-Cl	2.29 (1 bar)	10.17	8
PRP-1	2.09 (1 bar)	9.20	9
HCS-S	2.63 (1 bar)	11.57	10
OMC	3.00 (1 bar)	13.20	11
NAB-2	3.18 (1 bar)	14.20	12
mPTPA-2	2.41 (1 bar)	10.60	13
BoxPOP-2	1.25 (1 bar)	5.50	14
Al-PMOF	0.25 (1 bar)	1.10	15
MUF-16	2.23 (1 bar)	9.81	16

Table S3 The isosteric heat of adsorption Q_{st} of various samples

<i>Samples</i>	The isosteric enthalpy of adsorption Q_{st}	<i>Ref.</i>
BILPs	ca.28 kJ mol ⁻¹	17, 18
Azo-COPs	ca.24–29 kJ mol ⁻¹	19
TB-COP	25.9 kJ mol ⁻¹	20
ALPs	ca. 27–28 kJ mol ⁻¹	21
MAPOPs	ca. 18–30 kJ mol ⁻¹	22
Networks	ca. 25–26 kJ mol ⁻¹	23
<i>FZU-PTPA</i>	28.9–30.1kJ mol ⁻¹	<i>This work</i>

Table S4 kinetic parameters of the FZU-PTPA (120 °C) towards the mercury ions fitted by the pseudo-first-order and pseudo-second-order model

C ₀ (mg L ⁻¹)	Pseudo-first-order constants			Pseudo-second-order constants			
	q _e (mg g ⁻¹)	k ₁ (min ⁻¹)	R ²	q _e (mg g ⁻¹)	k ₂ (g mg ⁻¹ min ⁻¹)	h (g mg ⁻¹ min ⁻¹)	R ²
50	49	1.42	0.999	49	0.52	1250	0.999
200	170	1.02	0.992	175	0.008	250	0.999
400	414	0.971	0.980	435	0.002	370	1

Table S5 initial adsorption rate h of benchmark adsorbents

Adsorbent	initial adsorption rate h (mg g ⁻¹ min ⁻¹)	Ref.
FZU-PTPA	1203.65	this work
PANI-F-S	147.80	24
MMS/CS	478.47	25
Fe ₃ O ₄ @DTIM-MOF@SH	16.12	26
ZrSulf	5.31	27
Co-N-C	16.12	28
COF _{TFP-BTH}	71.43	29
PAF-SH	49.20	30
PAF-Sme	152.39	30
PSN-N ₂	27	31
MMS/MoS ₂	476	32

Table S6 isotherm parameters of the FZU-PTPA (120 °C) towards the mercury ions fitted by the Langmuir and Freundlich model

Temperature (°C)	Langmuir Model			Freundlich Model		
	q_m (mg g ⁻¹)	K_L (L g ⁻¹)	R^2	K_F (mg g ⁻¹)	n	R^2
25	1111	6.76	0.984	2.72	80.87	0.979
35	1250	9.12	0.994	2.67	92.31	0.947
45	1429	9.07	0.997	2.47	87.07	0.900

Table S7 Properties of cations used in competitive adsorption experiments.

Ions	Ionic radius (Å)	Stokes radius (Å)	Hydrated radius (Å)
Ni ²⁺	0.70	2.92	4.0
Co ²⁺	0.72	3.35	4.2
Pb ²⁺	1.32	2.83	4.0
Cu ²⁺	0.72	3.25	4.2
Zn ²⁺	0.74	3.49	4.3
La ³⁺	1.15	3.96	4.5
Hg ²⁺	0.69	-	3.0

Table S8 thermodynamic parameters of the FZU-PTPA (120 °C) towards the mercury ions

ΔH (kJ mol ⁻¹)	ΔS (J mol ⁻¹ K ⁻¹)	ΔG (kJ mol ⁻¹)		
		298 K	308 K	318 K
27.16	105.42	-4.26	-5.19	-5.96

Table S9 adsorption capacity towards the mercury ions of other advanced porous materials

Adsorbent	Q_{\max} (mg g ⁻¹)	Ref.
TAPB-BMTTPA-COF	734	33
TLMSM	954.7	34
MT-PNPs	297	35
COF-LZU8	236	36
PAF-1-SH	1014	37
MOF-808-SH	977.5	38
Fe ₃ O ₄ @DTIM-MOF@SH	756.9	26
PNE-S	971	39
Thiol functionalized porous organic polymer	1216	40
Fe ₃ O ₄ @TMU-32	905	41
FS@PTL-SH	1001.2	42
Bi-I-functionalized Fe ₃ O ₄ @SiO ₂ @HKUST-1	264	43
sulfur/reduced GO nanohybrid	908	44
SWCNT-SH	131	45
amide functionalized cellulose	178	46
MOP-SH	703	47
AzoPOP-SH	910	47
UiO-66-DMTD	670	48
SMP	595.2	49
MNPC	476	50
PTPA-120	1429	this work

Table S10 XPS N1s spectra information of FZU-PTPA synthesized under differential temperature.

	=N- / tertiary amine			-NH-		
	Peak position/eV	Peak area	Peak ratio $A_{(=N-)} / A_{sum}$	Peak position/eV	Peak area	Peak ratio $A_{(-NH-)} / A_{sum}$
100 °C	399.4	4344	0.49	399.9	4547	0.58
120 °C	399.4	9679	0.58	400	7018	0.42
140 °C	399.6	9342	0.58	400.2	6649	0.42
160 °C	399.5	8274	0.50	400	8185	0.50

Table S11 XPS C1s spectra information of FZU-PTPA synthesized under differential temperature.

	C–O/C=O			C=N			C–N			C–H/C–C		
	Peak position/eV	Peak area	Peak ratio	Peak position/eV	Peak area	Peak ratio	Peak position/eV	Peak area	Peak ratio	Peak position/eV	Peak area	Peak ratio
100 °C	287.5	1904	0.040	285.5	17942	0.366	284.8	17088	0.349	284.3	12042	0.245
120 °C	287.6	2586	0.031	285.6	27383	0.331	284.9	28152	0.341	284.3	24542	0.297
140 °C	287.6	3909	0.048	285.6	26152	0.320	284.9	27865	0.341	284.4	23796	0.291
160 °C	287.7	3918	0.047	285.7	27101	0.321	284.9	31086	0.369	284.3	22207	0.263

Table S12 XPS O1s spectra information of FZU-PTPA synthesized under differential temperature.

	O=C			C-O		
	Peak position/eV	Peak area	Peak ratio $A_{(O=C)}/A_{sum}$	Peak position/eV	Peak area	Peak ratio $A_{(C-O)}/A_{sum}$
100 °C	532.2	5426	0.88	533.7	725	0.12
120 °C	531.7	3801	0.38	533.1	6136	0.62
140 °C	531.7	6248	0.35	533.1	11396	0.65
160 °C	532.2	11733	0.60	533.8	78880	0.40

Table S13 XPS N1s spectra information of FZU-PTPA synthesized under differential pressure.

	=N- / tertiary amine			-NH-		
	Peak position/eV	Peak area	Peak ratio $A_{(=N-)} / A_{sum}$	Peak position/eV	Peak area	Peak ratio $A_{(-NH-)} / A_{sum}$
0 MPa	399.5	4487	0.48	400	4796	0.52
2 MPa	399.4	9679	0.58	400	7018	0.42

Table S14 XPS C1s spectra information of FZU-PTPA synthesized under differential pressure

	C-O/C=O			C=N			C-N			C-H/C-C		
	Peak position /eV	Peak area	Peak ratio	Peak position /eV	Peak area	Peak ratio	Peak position /eV	Peak area	Peak ratio	Peak position /eV	Peak area	Peak ratio
0 MP	287.7	3167	0.068	286.0	6406	0.136	285.3	11969	0.255	284.5	25406	0.541
2 MP	287.6	2586	0.031	285.6	27383	0.331	284.9	28152	0.341	284.3	24542	0.297

Table S15 XPS O1s spectra information of FZU-PTPA synthesized under differential pressure

	O=C			C-O		
	Peak position/eV	Peak area	Peak ratio $A_{(O=C)}/A_{sum}$	Peak position/eV	Peak area	Peak ratio $A_{(C-O)}/A_{sum}$
0 MPa	531.3	3332	0.32	532.5	7167	0.68
2 MPa	531.7	3801	0.38	533.1	6136	0.62

Table S16 XPS N1s spectra information of FZU-PTPA synthesized under differential reaction time

	=N- / tertiary amine			-NH-		
	Peak position/eV	Peak area	Peak ratio $A_{(=N-)} / A_{sum}$	Peak position/eV	Peak area	Peak ratio $A_{(-NH-)} / A_{sum}$
1 h	399.6	8549	0.50	400.2	8621	0.50
5 h	399.4	9679	0.58	400	7018	0.42

Table S17 XPS C1s spectra information of FZU-PTPA synthesized under differential reaction time

	C–O/C=O			C=N			C–N			C–H/C–C		
	Peak position/eV	Peak area	Peak ratio	Peak position/eV	Peak area	Peak ratio	Peak position/eV	Peak area	Peak ratio	Peak position/eV	Peak area	Peak ratio
1 h	287.6	3757	0.043	285.7	27990	0.323	285	28126	0.324	284.5	26873	0.310
5 h	287.6	2586	0.031	285.6	27383	0.331	284.9	28152	0.341	284.3	24542	0.297

Table S18 XPS O1s spectra information of FZU-PTPA synthesized under differential reaction time.

	O=C			C-O		
	Peak position/eV	Peak area	Peak ratio $A_{(O=C)}/A_{sum}$	Peak position/eV	Peak area	Peak ratio $A_{(C-O)}/A_{sum}$
1 h	531.5	4015	0.27	532.8	10794	0.73
5 h	531.7	3801	0.38	533.1	6136	0.62

Table S19 XPS N1s spectra information of PTPA-Cl

	=N- / tertiary amine			-NH-			-N ⁺ -			N-Cl		
	Peak position/eV	Peak area	Peak ratio	Peak position/eV	Peak area	Peak ratio	Peak position/eV	Peak area	Peak ratio	Peak position/eV	Peak area	Peak ratio
FZU-PTPA (120 °C)	399.4	9679	0.58	400	7018	0.42	N.A.	N.A.	N.A.	N.A.	N.A.	N.A.
PTPA-Cl	399.5	15701	0.23	400.1	23636	0.34	401.4	10303	0.15	402.3	19524	0.28

Table S20 XPS C1s spectra information of PTPA-Cl

	C-O/C=O			C-C=N			C-N			C-C		
	Peak position/eV	Peak area	Peak ratio	Peak position/eV	Peak area	Peak ratio	Peak position/eV	Peak area	Peak ratio	Peak position/eV	Peak area	Peak ratio
FZU-PTPA (120 °C)	287.6	2586	0.031	285.6	27383	0.331	284.9	28152	0.341	284.3	24542	0.297
PTPA-Cl	284.4	106533	0.313	284.9	108397	0.319	285.6	87932	0.259	286.5	36881	0.109

Table S21 XPS O1s spectra information of PTPA-Cl

	O=C			C-O		
	Peak position/eV	Peak area	Peak ratio	Peak position/eV	Peak area	Peak ratio
FZU-PTPA (120 °C)	531.7	3801	0.38	533.1	6136	0.62
PTPA-Cl	532.0	13939 2	0.60	533.2	95488	0.40

Table S22 XPS N1s spectra information of FZU-PTPA before and after adsorption with the mercury ion.

	=N- / tertiary amine			-NH-		
	Peak position/eV	Peak area	Peak ratio $A_{(=N-)} / A_{sum}$	Peak position/eV	Peak area	Peak ratio $A_{(-NH-)} / A_{sum}$
Before adsorption	399.4	9679	0.58	400	7018	0.42
After adsorption	N.A.	N.A.	N.A.	399.8	13709	1

Table S23 XPS C1s spectra information of FZU-PTPA before and after adsorption with the mercury ion

	C–O/C=O			C=N			C–N			C–H/C–C		
	Peak position/eV	Peak area	Peak ratio	Peak position /eV	Peak area	Peak ratio	Peak position /eV	Peak area	Peak ratio	Peak position /eV	Peak area	Peak ratio
Before adsorption	287.6	2586	0.031	285.6	27383	0.331	284.9	28152	0.341	284.3	2454 2	0.29 7
After adsorption	287.2	5980	0.088	285.5	29534	0.437	284.8	20330	0.301	284.3	1173 7	0.17 4

Table S24 XPS O1s spectra information of FZU-PTPA before and after adsorption with the mercury ion

	O=C			C-O		
	Peak position/eV	Peak area	Peak ratio $A_{(O=C)}/A_{sum}$	Peak position/eV	Peak area	Peak ratio $A_{(C-O)}/A_{sum}$
Before adsorption	531.7	3801	0.38	533.1	6136	0.62
After adsorption	531.6	6884	0.34	533.1	10230	0.66

References:

1. N. Graf, E. Yegen, T. Gross, A. Lippitz, W. Weigel, S. Krakert, A. Terfort and W. E. S. Unger, *Surf. Sci.*, 2009, **603**, 2849-2860.
2. S. Golczak, A. Kanciużewska, M. Fahlman, K. Langer and J. J. Langer, *Solid State Ion.*, 2008, **179**, 2234-2239.
3. Y. Li, Q. Chen, T. Xu, Z. Xie, J. Liu, X. Yu, S. Ma, T. Qin and L. Chen, *J. Am. Chem. Soc.*, 2019, **141**, 13822-13828.
4. P. N. Adams, P. J. Laughlin, A. P. Monkman and A. M. Kenwright, *Poly.*, 1996, **37**, 3411-3417.
5. P. N. Adams and A. P. Monkman, *Synth. Met.*, 1997, **87**, 165-169.
6. A. Ohtani, M. Abe, M. Ezoe, T. Doi, T. Miyata and A. Miyake, *Synth. Met.*, 1993, **57**, 3696-3701.
7. J. Wang, W. Sng, G. Yi and Y. Zhang, *Chem. Comm.*, 2015, **51**, 12076-12079.
8. O. Buyukcakir, S. H. Je, D. S. Choi, S. N. Talapaneni, Y. Seo, Y. Jung, K. Polychronopoulou and A. Coskun, *Chem. Comm.*, 2016, **52**, 934-937.
9. M. Ding and H.-L. Jiang, *Chem. Comm.*, 2016, **52**, 12294-12297.
10. X. Li, S. Bai, Z. Zhu, J. Sun, X. Jin, X. Wu and J. Liu, *Langmuir*, 2017, **33**, 1248-1255.
11. B. Yuan, X. Wu, Y. Chen, J. Huang, H. Luo and S. Deng, *Environ. Sci. Technol.*, 2013, **47**, 5474-5480.
12. O. Buyukcakir, S. H. Je, J. Park, H. A. Patel, Y. Jung, C. T. Yavuz and A. Coskun, *Chem. Eur. J.*, 2015, **21**, 15320-15327.
13. X. Hu, H. Wang, C. F. J. Faul, J. Wen, Y. Wei, M. Zhu and Y. Liao, *Chem. Eng. J.*, 2020, **382**, 122998.
14. S. Xu, J. He, S. Jin and B. Tan, *J. Colloid and Interface Sci.*, 2018, **509**, 457-462.
15. P. G. Boyd, A. Chidambaram, E. Garcia-Diez, C. P. Ireland, T. D. Daff, R. Bounds, A. Gladysiak, P. Schouwink, S. M. Moosavi, M. M. Maroto-Valer, J. A. Reimer, J. A. R. Navarro, T. K. Woo, S. Garcia, K. C. Stylianou and B. Smit, *Nature*, 2019, **576**, 253-256.
16. O. T. Qazvini, R. Babarao and S. G. Telfer, *Nat. Commun.*, 2021, **12**, 197.
17. O. K. Farha, A. M. Spokoyny, B. G. Hauser, Y.-S. Bae, S. E. Brown, R. Q. Snurr, C. A. Mirkin and J. T. Hupp, *Chem. Mater.*, 2009, **21**, 3033-3035.
18. M. G. Rabbani and H. M. El-Kaderi, *Chem. Mater.*, 2011, **23**, 1650-1653.
19. H. A. Patel, S. Hyun Je, J. Park, D. P. Chen, Y. Jung, C. T. Yavuz and A. Coskun, *Nat. Commun.*, 2013, **4**, 1357.
20. J. Byun, S.-H. Je, H. A. Patel, A. Coskun and C. T. Yavuz, *J. Mater. Chem. A*, 2014, **2**, 12507-12512.
21. P. Arab, M. G. Rabbani, A. K. Sekizkardes, T. İslamoğlu and H. M. El-Kaderi, *Chem. Mater.*, 2014, **26**, 1385-1392.
22. X. Ding, H. Li, Y.-C. Zhao and B.-H. Han, *Polym. Chem.*, 2015, **6**, 5305-5312.
23. R. Dawson, E. Stöckel, J. R. Holst, D. J. Adams and A. I. Cooper, *Energy Environ. Sci.*, 2011, **4**, 4239-4245.
24. S. A. Hashemi, S. M. Mousavi and S. Ramakrishna, *J. Clean. Prod.*, 2019, **239**.
25. H. He, X. Meng, Q. Yue, W. Yin, Y. Gao, P. Fang and L. Shen, *Chem. Eng. J.*, 2021, **405**, 126743.

26. Y. Li, M. Tan, G. Liu, D. Si, N. Chen and D. Zhou, *J. Mater. Chem. A*, 2022, **10**, 6724-6730.
27. J. Li, X. Li, A. Alsaedi, T. Hayat and C. Chen, *J. Colloid. Interface Sci.*, 2018, **517**, 61-71.
28. L. Xing, M. Li, T. Qi, L. Mao, Z. Hu, E. Zhang, G. P. Hao, B. Mao and L. Wang, *Environ. Sci. Technol.*, 2022, **56**, 4531-4541.
29. L. Wang, Y. Song, Y. Luo and L. Wang, *J. Ind. Eng. Chem.*, 2022, **106**, 374-381.
30. X. Liao, G. Yu, R. Luo, Q. Wang, C. He and S. Liu, *J. Hazard. Mater.*, 2021, **418**, 126244.
31. Q. Ge and H. Liu, *Chem. Eng. J.*, 2022, **428**, 131370.
32. P. Gao, J. Lei, J. Tan, G. Wang, H. Liu and L. Zhou, *Compos. Commun.*, 2021, **25**.
33. N. Huang, L. Zhai, H. Xu and D. Jiang, *J. Am. Chem. Soc.*, 2017, **139**, 2428-2434.
34. K. Fu, X. Liu, C. Lv, J. Luo, M. Sun, S. Luo and J. C. Crittenden, *Environ. Sci. Technol.*, 2022, **56**, 2677-2688.
35. Y. Z. Fan, L. Han, Y. Z. Yang, Z. Sun, N. Li, B. L. Li, H. Q. Luo and N. B. Li, *Environ. Sci. Technol.*, 2020, **54**, 10270-10278.
36. S.-Y. Ding, M. Dong, Y.-W. Wang, Y.-T. Chen, H.-Z. Wang, C.-Y. Su and W. Wang, *J. Am. Chem. Soc.*, 2016, **138**, 3031-3037.
37. B. Li, Y. Zhang, D. Ma, Z. Shi and S. Ma, *Nat. Commun.*, 2014, **5**, 5537.
38. C. Ji, Y. Ren, H. Yu, M. Hua, L. Lv and W. Zhang, *Chem. Eng. J.*, 2022, **430**, 132960.
39. Y. Kim, Z. Lin, I. Jeon, T. Van Voorhis and T. M. Swager, *J. Am. Chem. Soc.*, 2018, **140**, 14413-14420.
40. B. Aguila, Q. Sun, J. A. Perman, L. D. Earl, C. W. Abney, R. Elzein, R. Schlaf and S. Ma, *Adv. Mater.*, 2017, **29**, 1700665.
41. N. Abdollahi, S. A. Akbar Razavi, A. Morsali and M.-L. Hu, *J. Hazard. Mater.*, 2020, **387**, 121667.
42. Y. Sun, Y. Gu, X. Li and R. P. Singh, *React. Funct. Polym.*, 2022, **170**, 105129.
43. L. Huang, M. He, B. Chen and B. Hu, *J. Mater. Chem. A*, 2015, **3**, 11587-11595.
44. Suman, Thakur, Gautam, Das, Prasanta, Kumar, Raul, Niranjana and Karak, *J. Phys. Chem. B*, 2013.
45. N. M. Bandaru, N. Reta, H. Dalai, A. V. Ellis, J. Shapter and N. H. Voelcker, *J. Hazard. Mater.*, 2013, **261**, 534-541.
46. N. Sun, X. Wen and C. Yan, *Int. J. Biol. Macromol.*, 2018, **108**, 1199-1206.
47. L. Huang, C. Peng, Q. Cheng, M. He, B. Chen and B. Hu, *Ind. Eng. Chem. Res.*, 2017, **56**, 13696-13703.
48. L. Fu, S. Wang, G. Lin, L. Zhang, Q. Liu, J. Fang, C. Wei and G. Liu, *J. Hazard. Mater.*, 2019, **368**, 42-51.
49. D. Xu, W. D. Wu, H.-J. Qi, R.-X. Yang and W.-Q. Deng, *Chemosphere*, 2018, **196**, 174-181.
50. L. Huang, M. He, B.-b. Chen, Q. Cheng and B. Hu, *ACS Appl. Mater.*, 2017, **9**, 2550-2559.